LA-UR-21-25932
Approved for public release; distribution is unlimited.

Title: Validation of a Pressure Dependent PBX 9501 Cookoff Model

Author(s): Aviles-Ramos, Cuauhtemoc
Hobbs, M. L.

Intended for: Report

Issued: 2021-06-23

Disclaimer:
Los Alamos National Laboratory, an affirmative action/equal opportunity employer, is operated by Triad National Security, LLC for the National Nuclear Security Administration of U.S. Department of Energy under contract 89233218CNA000001. By approving this article, the publisher recognizes that the U.S. Government retains nonexclusive, royalty-free license to publish or reproduce the published form of this contribution, or to allow others to do so, for U.S. Government purposes. Los Alamos National Laboratory requests that the publisher identify this article as work performed under the auspices of the U.S. Department of Energy. Los Alamos National Laboratory strongly supports academic freedom and a researcher's right to publish; as an institution, however, the Laboratory does not endorse the viewpoint of a publication or guarantee its technical correctness.

Validation of a Pressure Dependent PBX 9501 Cookoff Model

Aviles-Ramos*, C., Hobbs#, M. L.

*Advanced Engineering Analysis, W-13, Los Alamos National Laboratory, Los Alamos New Mexico 87545.

#Engineering Sciences Center, Sandia National Laboratories, Albuquerque, New Mexico, 87105.

Abstract

A pressure dependent cookoff model for PBX 9501 was developed by Hobbs' et al. [1]. This cookoff model was implemented in the finite element (FE) heat transfer code Aria [2] and was used to simulate a set of cookoff experiments. This set is called the Large Scale Annular Cookoff (LSAC) experiments [3]. Three dimensional and axisymmetric heat conduction FE models were implemented to simulate these experiments. The predictive ability of the PBX 9501 pressure dependent cookoff model was evaluated using Latin Hypercube sampling (LHS). Predictions of the thermal times to ignition and temperatures are compared with the experiments.

Keywords: Ignition kinetics, Thermal runaway, Non-linear heat conduction, Energetic materials.

Description of the LSAC Experiments

The LSAC experiments [3] consist of PBX 9501 annular cylinders confined by two copper liners. Figure 1 shows a sketch for this apparatus. The outer surface of the outer liner is heated using electric heaters (see Fig. 2) that produce prescribed temperature ramps until soak temperatures (ST) are reached. The last ST is kept constant until thermal ignition occurs. Thermocouples are used to measure external temperatures on the inner liner, outer liner, and end caps. Also, internal temperatures are measured at the mid-plane where two PBX 9501 cylindrical halves meet. Figure 3 shows a photo of the internal thermocouples installed at the midplane. A diagram for the location of the midplane and boundary thermocouples is given in Figure 4. Thermocouples 1 to 6 (shown in Fig. 4 in blue) were used to define the boundary condition temperatures on the outer liner and thermocouples 7 to 12 (shown in Fig. 4 in blue) were used to define the boundary condition temperatures on the inner liner. Thermocouples 1 to 18 (shown in Fig. 4 in red) represent the internal temperature measurements at the midplane. There were 8 LSAC

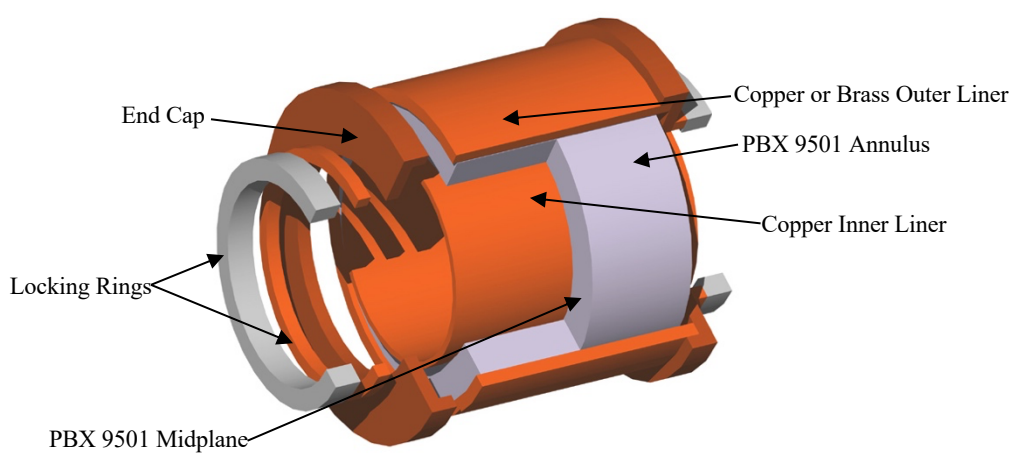

Figure 1. Schematic of LSAC [3] assembly

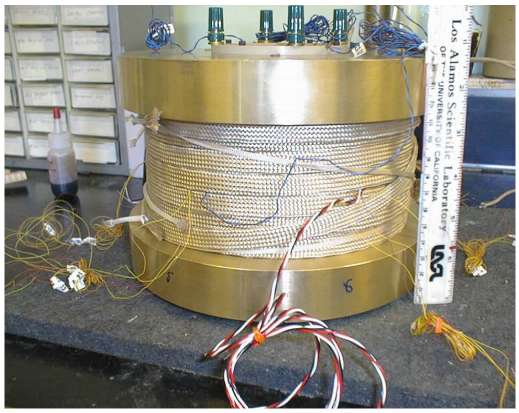

Figure 2. Electric heaters on outer liner for LSAC [3].

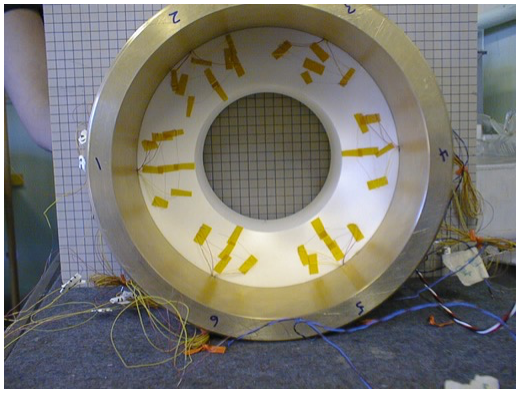

Figure 3. Thermocouples installed at the midplane were the two PBX 9501 cylindrical halves meet.

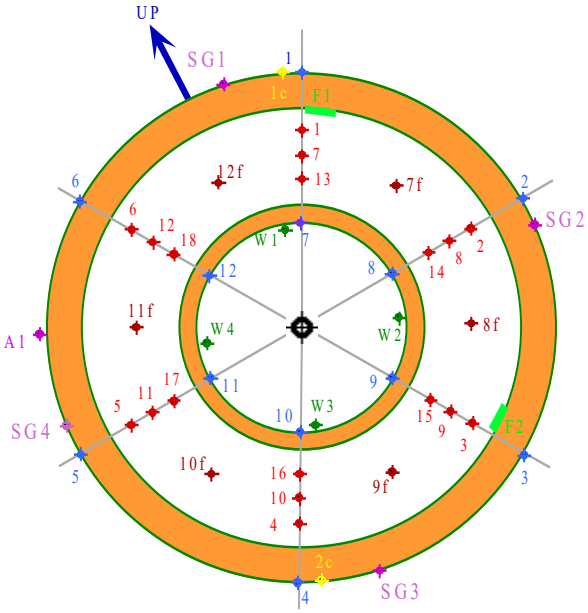

Figure 4. Schematic for midplane and boundary thermocouples location for LSAC shots 5, 6, 7, and 8.

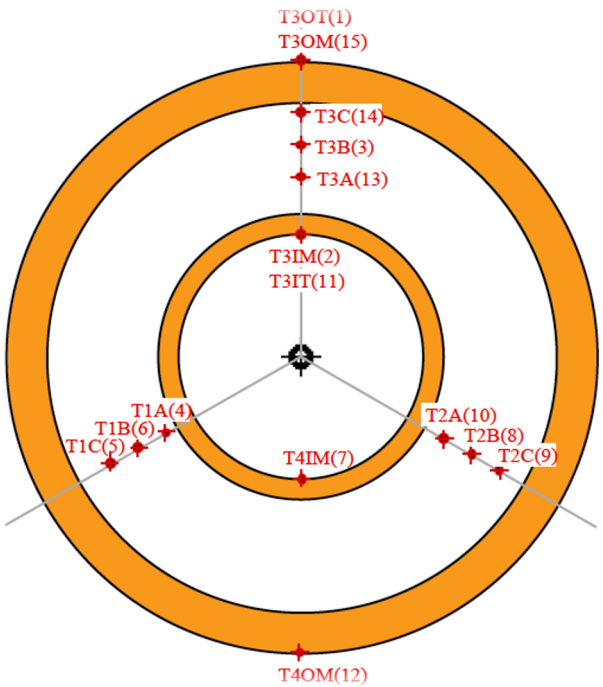

Figure 5. Schematic for midplane and boundary thermocouples locations for LSAC shot 1. No end caps thermocouples were used for this shot.

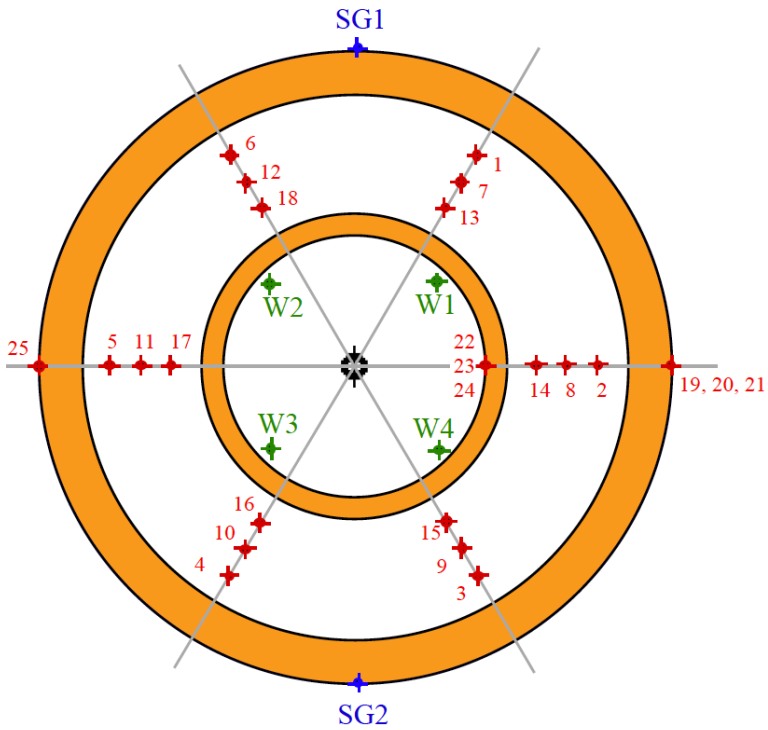

Figure 6. Schematic for midplane and boundary thermocouples locations representative of LSAC shots 2 and 3. No end caps thermocouples were used for this shot.

shots. The internal and external thermocouples installed for shot 1 are shown in Fig. 5. Note from Fig. 5 that only two external thermocouple locations were planned to define boundary conditions on the inner and outer liners. Also, shot 1 only had 9 internal thermocouples installed on the PBX 9501 midplane. Figure 6 shows a schematic that applies for the thermocouples installed in shots 2 and 3. Note from Fig. 6 that external temperatures were measured only at one or two locations on the inner and outer liners. Figure 6 also shows that eighteen internal thermocouples were installed at the midplane for shots 2 and 3. No end caps thermocouples were installed for shots 1 to 4. End caps thermocouples were installed for shot 5 to 8. Also, shots 5 to 8 had the largest number of external thermocouples. Six thermocouples on the outer liner and six thermocouples on the inner liner (Fig. 4). These twelve external thermocouples permitted a more accurate definition of the boundary conditions for shots 5 to 8.

Shot 4 was preheated for a period of 6480 s. The actual cookoff experiment was started after this preheating period. For this reason, the initial temperatures in the metal and PBX 9501 parts were nonuniform ranging from 75 °C to 82 °C. This variability introduces significant uncertainty in the initial conditions that could be used to model this experiment. In addition, the external temperatures on the outer and inner liner were measured at one circumferential location only. Since the external temperatures were nonuniform after the preheating phase, and these temperatures were measured at only two locations, this lack of boundary temperature information introduces significant uncertainty in the boundary conditions that could be used to model this experiment. For these reasons, shot 4 was not modeled in this study.

Figure 7 shows the thermocouple readings that were used to define the boundary conditions for the simulation of shot 7. Note that there is significant variation for one of the outer liner thermocouples in Fig. 7. This is due to the heater effects. User subroutines were written to apply the boundary conditions on the inner and outer liners as functions of the circumferential angle.

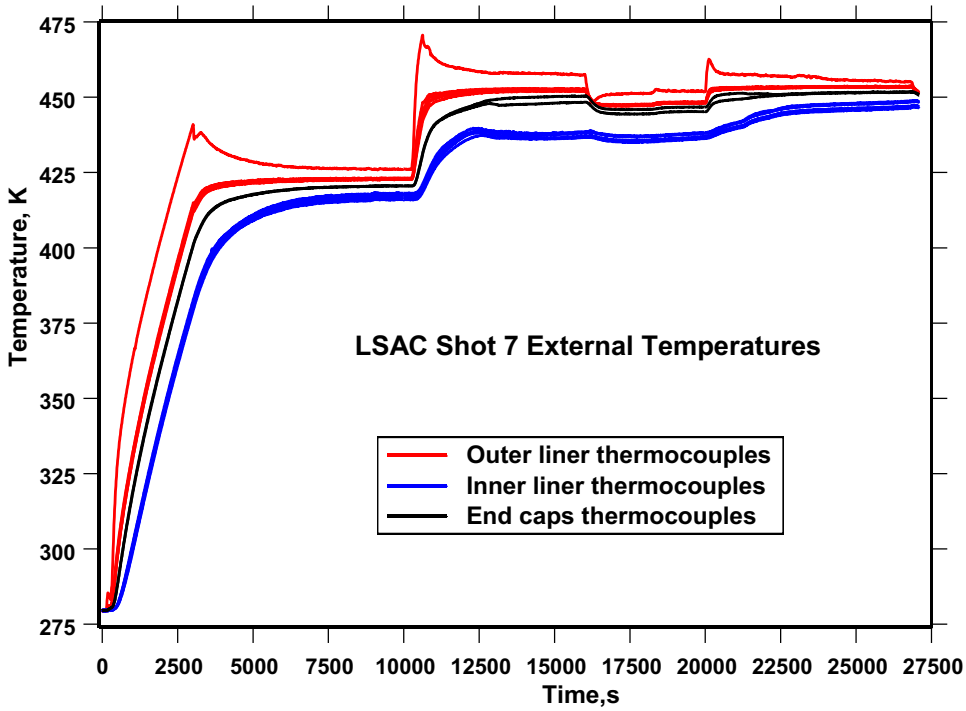

Figure 7. Measured boundary conditions for LSAC shot 7 [3].

The time to thermal ignition is the primary variable used for these comparisons. Table 1 shows the experimental times to thermal ignition for the simulated LSAC tests.

Table 1. Thermal ignition times for 7 LSAC cook-off experiments.

Experiment	Experimental Time to Ignition, s
shot 1	25081
shot 2	45535
shot 3	37689
shot 5	26205
shot 6	20515
shot 7	27090
shot 8	29865

The Hobbs' et al. PBX 9501 Cookoff Model

This section gives a brief description of the thermal ignition model for PBX 9501. Details of this model have been presented in the literature [1] and is described briefly in the current work. PBX 9501 is composed of HMX and a reactive binder. The HMX decomposition mechanism is a simplification of the mechanism proposed by Behrens and Maharrey [4], wherein the HMX is assumed to react in the gas, solid, and molten phases. The binder is also assumed to decompose similarly to the HMX. Interaction between the explosive and binder occurs through the nitroplasticizer, which decomposes into reaction NOx products, assumed to be NO_2.

The decomposition mechanism is presented in Table 2. Adsorbed gases are assumed to be moisture that evolve in a first order, diffusion limited reaction (See Eq. 2). Diffusion is implanted by the form of the rate equation given in Eq. (7), which uses a distributed activation energy. For this reaction, the distribution parameter (σ_1/R, see Table 4) is positive, which implies that the activation energy increases with the extent of reaction, which mimics diffusion resistance. Conversely, the distribution parameters for the remaining reactions (σ_2/R, σ_3/R, σ_4/R, σ_5/R) are negative, which causes the activation energy to drop as the reactions proceed, similar to an autocatalytic reaction.

The model uses molar concentrations in the reaction rates. Also, interaction occurs between the binder and explosives via formation of NO_2 (oxidizer) and reaction of the NO_2 with the fuels (Estane® and HMX). The reaction of Estane® with NO_2 forms equilibrium products. Likewise, the HMX reactions are assumed to form final equilibrium products at typical cookoff conditions.

The cookoff model is sensitive to pressure. The auxiliary equations show how pressure is calculated using the BKW equation-of-state (EOS) [5]. However, in our analysis, the pressures are low enough that the ideal gas equation-of-state (EOS) is sufficient with the compressibility (z) being equal to one. Pressure is implemented into the model using a pressure rate multiplier $(P/P_o)^n$. The model is sensitive to the pressure. When the experiments are vented, the pressure exponents (n_i) are set to zero.

Determination of the pressure is often difficult, especially when the PBX 9501 is near the theoretical maximum density (TMD). At these high densities, the gas volume fraction (Eq. 19) is small, and the permeability is low. In fact, we expect the pores to be closed when the density approaches TMD. Thus, at high densities, it is difficult to determine the pressure. If the porosity

is open, then the gases can escape, and the pressure used in the reaction rates are lower than if the porosity is closed. This model bounds most cookoff data by using both the vented option (n_i set to zero) and sealed option (n_i as given in Table 4). The challenge is to determine, what the pressure is, which could be a function of the thermal damage in the form of porosity and permeability. Table 2 presents the PBX 9501 decomposition model.

TABLE 2. PBX 9501 ignition model[a]

Energy conservation	$\nabla \cdot (k\,\nabla T) + \sum_{i=1}^{5} r_i\, h_{r_i}\, M_{w,i} = \rho_b C_b \dfrac{\partial T}{\partial t}$	(1)
Mechanism	$H_2O_a \xrightarrow{1} H_2O_g$	(2)
	$\text{BDNPA/F} \xrightarrow{2} \text{NVR} + 4NO_2$	(3)
	$\text{Estane} + NO_2 \xrightarrow{3} 7.1\ \text{Gas}_E + 8.1\ \text{Carbon}$	(4)
	$\text{HMX} + NO_2 \xrightarrow{4} 11.5\ \text{Gas}_{x1} + \text{Carbon}$	(5)
	$\text{HMX} \xrightarrow{5} 10\ \text{Gas}_{x2} + 1.6\ \text{Carbon}$	(6)
	$r_1 = A_1 \exp\left(\dfrac{-E_1 + \xi\,\sigma_1}{RT}\right)[H_2O]$	(7)
	$r_2 = \zeta\, A_2 \exp\left(\dfrac{-E_2 + \xi\,\sigma_2}{RT}\right)[\text{BDNPA/F}]$	(8)
	$r_3 = \zeta\, A_3 \left(\dfrac{P}{P_0}\right)^{n_3} T^{m_3} \exp\left(\dfrac{-E_3 + \xi\,\sigma_3}{RT}\right)[\text{Estane}][NO_2]$	(9)
	$r_4 = \zeta\, A_4 \left(\dfrac{P}{P_0}\right)^{n_4} T^{m_4} \exp\left(\dfrac{-E_4 + \xi\,\sigma_4}{RT}\right)[\text{HMX}][NO_2]$	(10)
	$r_5 = \zeta\, A_5 \left(\dfrac{P}{P_0}\right)^{n_5} T^{m_5} \exp\left(\dfrac{-E_5 + \xi\,\sigma_5}{RT}\right)[\text{HMX}]$	(11)
Species conservation	$\frac{d[H_2O_a]}{dt} = -r_1;\ \frac{d[H_2O_g]}{dt} = r_1;\ \frac{d[\text{BDNPA/F}]}{dt} = -r_2;\ \frac{d[\text{NVR}]}{dt} = r_2;\ \frac{d[NO_2]}{dt} = 4r_2 - r_3 - r_4$	(12)
	$\frac{d[\text{Estane}]}{dt} = -r_3;\ \frac{d[\text{Gas}_E]}{dt} = 7.1 r_3;\ \frac{d[\text{Carbon}]}{dt} = 8.1 r_3 + r_4 + 1.6 r_5$	
	$\frac{d[\text{HMX}]}{dt} = -r_4 - r_5;\ \frac{d[\text{Gas}_{X1}]}{dt} = 11.5 r_4;\ \frac{d[\text{Gas}_{X2}]}{dt} = 10 r_5$	

Distribution parameter,[b] ξ	$P_1 = \frac{[H_2O]}{\omega_{H_2O_a}\rho_{b,o}/Mw_{H_2O_a}}$; $P_2 = \frac{[\text{BDNPA/F}]}{\omega_{\text{BDNPA/F}}\rho_{b,o}/Mw_{\text{BDNPA/F}}}$; $P_2 = \frac{[\text{Estane}]}{\omega_{\text{Estane}}\rho_{b,o}/Mw_{\text{Estane}}}$	(13)
	$P_4 = P_5 = \frac{[\text{HMX}]}{\omega_{\text{HMX}}\rho_{b,o}/Mw_{\text{HMX}}}$	

[a]Nomenclature and model parameters are given in Table 4.

[b]$\xi = \text{norminv}(P_i)$, where "norminv" is the inverse of the standard normal cumulative distribution function that has a mean of 0 and a standard deviation of 1.

TABLE 3. Auxiliary equations used to calculate the thermodynamic pressure[a]

Pressure	$P = \frac{znRT_{ave}}{V_g}$	(14)
Compressibility	$z = 1 + X\exp(\beta X)$, where $X = \frac{nk\sum x_i k_i}{v_g(T_{ave}+\theta)^{\alpha}}$	(15)
Gas moles	$n = \int_V \left([\text{H}_2\text{O}_g] + [\text{NO}_2] + [\text{Gas}_\text{E}] + [\text{Gas}_{\text{x1}}] + [\text{Gas}_{\text{x2}}]\right) dV$	(16)
Ave. gas temperature	$T_{ave} = \frac{\int_V \rho C T\, dV}{\int_V \rho C\, dV}$	(17)
Gas volume	$V_g = \int_V \phi\, dV$	(18)
Gas volume fraction	$\phi = 1 - \frac{S_f \rho_{c,o}(1-\phi_o)}{\rho_c}$	(19)
Reacted solid fraction	$S_f = \frac{[\text{H}_2\text{O}_g]Mw_{\text{H}_2\text{O}_a} + [\text{BDNPA/F}]Mw_{\text{BDNPA/F}} + [\text{NVR}]Mw_{\text{NVR}} + [\text{Estane}]Mw_{\text{Estane}} + [\text{Carbon}]Mw_{\text{Carbon}} + [\text{HMX}]Mw_{\text{HMX}}}{\rho_{b,0}}$	(20)
Condensed density	$\rho_c = \rho_{c,o}\left[1 - 0.000131(T - T_o)\right]$, when $T \le T_{\beta \text{ to } \delta}$	(21)
	$\rho_c = \rho_{c,o}\left\{\left[1 - 0.000131(T - T_o)\right] - 0.067\right\}$, when $T > T_{\beta \text{ to } \delta}$	

[a]Nomenclature and model parameters are given in Table 3.

TABLE 4. Nomenclature and model parameters

Symbols	Description	Value	Units
Ln(A_1), Ln(A_2), Ln(A_3), Ln(A_4), Ln(A_5)	Natural logarithm of the pre-exponential factors	35, 35, 35, 35	Ln($s^{-1}K^{-n}$)
α	BKW constant	0.5	K^{-1}
β	BKW constant	0.298	none
β_V	Thermal expansion coefficient	0.000131	$(m^3/m^3)K^{-1}$
[BDNPA/F]	NP concentration	Initially $\omega_{BDNPA/F} \times \rho_{bo}/M_{w,BDNPA/F}$	$kgmol/m^3$
C	Specific Heat	below 250 K: 919 above 700 K: 2406 250 to 700 K: 92.93+3.305×T,K	$Jkg^{-1}K^{-1}$
$C_{eff,\ \beta\ to\ \delta}$	Effective capacitance for β to δ phase change using $h_{latent,\ \beta\text{-}\delta}$	441 K: 1550 444 K: 12560 447 K: 1570	$Jkg^{-1}K^{-1}$
$C_{eff,\ HMX\ melt}$	Effective capacitance for HMX melting phase change using $h_{latent,\ melt}$	527 K: 1835 530 K: 80511 533 K: 1854	$Jkg^{-1}K^{-1}$
C_E	Carbon from Estane® oxidation	Symbol used in mechanism	none
C_{x1}	Carbon from HMX oxidation	Symbol used mechanism	none
C_{x2}	Carbon from HMX decomposition	Symbol used mechanism	none
C_b	Bulk specific heat	See "C" above	$Jkg^{-1}K^{-1}$
[Carbon]	Carbon concentration from all reactions	Initially 0	$kgmol/m^3$

E_1/R, E_2/R, E_3/R, E_4/R, E_5/R	Activation energies divided by R	25500, 20400, 14350, 13600, 14625	K
[Estane]	Estane concentration	Initially $\omega_{Estane}\times\rho_{bo}/M_{w,Estane}$	kgmol/m^3
ϕ	Gas volume fraction	Field variable	m^3/m^3
ϕ_o	Initial gas volume fraction	$1-\rho_{bo}/\rho_{co}$	m^3/m^3
[Gas_E]	Gas conc. from Estane® oxidation	Initially 0	kgmol/m^3
[Gas_{x1}]	Gas conc. from HMX oxidation	Initially 0	kgmol/m^3
[Gas_{x2}]	Gas conc. from HMX decomposition	Initially 0	kgmol/m^3
[H_2O_a]	Adsorbed water concentration	Initially $\omega_{H2Oa}\times\rho_{bo}/M_{w,H2Oa}$	kgmol/m^3
[H_2O_g]	Desorbed water concentration	Initially 0	kgmol/m^3
$h_{f,i}$ where i= H_2O_a, H_2O_g, BDNPA/F, NVR, NO_2, Estane, G_E, Carbon, HMX, G_{X1}, G_{X2}	Heat of formation of species	-285.8×10^6, -241.8×10^6, -619.2×10^6, -1400×10^6, 34.2×10^6, -773×10^6, -195.7×10^6, 0×10^6, 75×10^6, -186.8×10^6,-175.1×10^6	Jkgmol^{-1}
$h_{latent,\beta\text{-}\delta}$	Latent enthalpy for β-δ phase change	33000	J kg^{-1}
$h_{latent,m}$	Latent enthalpy for HMX melt	236000	J kg^{-1}
i	ith reaction	1, 2, 3, 4, 5	none
κ	BKW constant	10.5×10^{-3}	Å^{-3}m^{3}kgmol^{-1}K$^{\alpha}$
$\Sigma x_i k_i$	Average BKW covolume factor. The covolume is the volume swept out by the molecule rotating about its center of mass. The covolume	447	Å^{-3}

	factor is the covolume multiplied by 9.43.		
k	β-HMX thermal conductivity is only a function of density. k changes linearly between β and δ phase between 441 K and 447 K.	860 kg/m^3: 0.12 1582 kg/m^3: 0.25 1778 kg/m^3: 0.33 Linear interpolation between densities	Wm^{-1}K^{-1}
k	δ-HMX thermal conductivity is only a function of density. k changes linearly between β and δ phase between 441 K and 447 K.	860 kg/m^3: 0.10 1582 kg/m^3: 0.19 1778 kg/m^3: 0.21 Linear interpolation between densities	Wm^{-1}K^{-1}
m_1, m_2, m_3, m_4, m_5	Steric factor for reactions 1 to 5	0, 0, -2, -2, -2	K^{-1}
$M_{w,i}$, where i= H_2O_a, H_2O_g, BDNPA/F, NVR, NO_2, Estane, G_E, Carbon, HMX, G_{X1}, G_{X2}	Molecular weight of species	18, 18, 319, 135, 46, 312, 20.4, 12, 296.2, 28.7, 27.6	kg/kgmol
n	Moles of gas	Field variable (Eqn. 16)	kgmol
n_1, n_2, n_3, n_4, n_5	Pressure exponent for reactions 1-5	0, 0, 1, 2, 0.2	none
[NO_2]	Nitric dioxide concentration	Initially 0	kgmol/m^3
norminv	Inverse of the standard normal distribution	function	none
[NVR]	Non-volatile-residue concentration	Initially 0	kgmol/m^3
P	Pressure	Initially 0	MPa (psig)

P_i (where i = 1, 5)	Progress of reaction 1 and 5	Field variable (Eqn. 13)	kgmol/kgmol
P_o	Initial pressure	0.08 (12.1) SITI, 0.1 (14.7) ODTX	MPa (psia)
θ	BKW constant	6620	K
ρ	Bulk density	Field variable	kgm^{-3}
$\rho_{b,o}$	Initial bulk density	SITI molding powder: 856 SITI lightly pressed: 1582 SITI fully pressed: 1779 ODTX: 1787 STEX: 1847 NAWC-Pipe: 1825 CSAFE-pipe: 1840 LASC: 1840 U-sphere: 1840	kgm^{-3}
ρ_c	Condensed density	Field variable (Eqn. 21)	kgm^{-3}
$\rho_{c,o}$	Initial condensed density (TMD)	1860	kgm^{-3}
R	Gas constant	0.08206	$m^3 atm\ kgmol^{-1}\ K^{-1}$
R	Gas constant	8314	$J\ kgmol^{-1} K^{-1}$
σ_1/R, σ_2/R, σ_3/R, σ_4/R, σ_5/R	Distribution parameters divided by R	2500, -200, -500, -2000, -1000	K
S_f	Reacted solid fraction	Field variable	kg/kg
T	Temperature	Field variable	K
T_{ave}	Average gas temperature	Global variables	K
$T_{\beta\text{-}\delta}$	β to δ phase change temperature	444 (normal distribution over 441-447)	K
T_{melt}	HMX melting temperature	530 (normal distribution over 527-533)	K
T_o	Initial temperature	Average SITI is 294.8 K	K
V_g	Gas volume	Global variable from Eqn. 18	m^3

V_{EM}	Volume of the energetic material	SITI molding powder: 15.82×10^{-6} SITI pressed pellets: 12.87×10^{-6} ODTX: 1.073×10^{-6} STEX: 412.0×10^{-6} NAWC-pipe: 19.71×10^{-6} CSAFE-pipe: 772.2×10^{-6} LASC: 1380×10^{-6} U-sphere: 231.7×10^{-6}	m^3
$\omega_{BDNPA/F}$	Mass fraction of NP	No migration: 0.025 Correlation for migration: $(1.63-0.00073\times\rho_{bo})\times0.025$	kg/kg
ω_{Estane}	Mass fraction of Estane®	No migration: 0.025 Correlation for migration: $(1.63-0.00073\times\rho_{bo})\times0.025$	kg/kg
ω_{H2Oa}	Mass fraction of adsorbed water	Initially 0.005	kg/kg
ω_{HMX}	Mass fraction of HMX	Initially $0.95-\omega_{H2Oa}$	kg/kg
X	Part of BKW equation	Defined in Eqn. 15	none
x_i, where $i = N_2, H_2O, CO_2, CH_4$	Gas mole fractions for HMX reaction	0.4, 0.36, 0.22, 0.02	mole/mole
ξ	norminv	Field variable	none
ξ_i	norminv for i^{th} reaction	Field variable	none
ζ	Melt rate acceleration factor	1+0.5*(1+tanh(T-530))*100	none
z	Compressibility	Global variables (Eqn. 15)	none

The cookoff model defined in Tables 2, 3, and 4 was implemented in Aria [2]. This implementation used FE integration points-based Encore [7] function calls to calculate pressure using the auxiliary equations defined in Table 3. The chemistry equations were solved using CHEMEQ [2] and the available Ordinary Differential Equations (ODE) solvers in Aria. The mesh of the LSAC experiments was constructed using Cubit [7]. An axisymmetric mesh was implemented for shots 1 to 3. A three-dimensional mesh was constructed for shots 5 and 6, and an additional three-dimensional mesh was constructed for shots 7 and 8. The LSAC shots 1 to 6 contained a PBX 9501 annulus with a length of 4 in, an inner radius of 1.75 in, and an outer radius of 3.125 in. Also, shots 7 and 8 contained a PBX 9501 annulus with a length of 8 in, an inner radius of 4 in, and an outer radius of 5.375 in.

Latin Hypercube Sampling Using the LSAC Experiments

Three dimensional and axisymmetric FE models of the PBX 9501 in the LSAC experiements were used with the LHS technique to estimate the uncertainty of the predicted temperatures and times to thermal ignition. McKay et al. [8] developed the LHS which is a smart sampling technique similar to a Monte Carlo uncertainty analysis and it is used to propagate uncertainty into the predicted results. The LHS samples used by the model were generated using a sensitivity analysis software called DAKOTA [9]. The linear standard correlation coefficient (Pearson's correlation coefficient) was used to calculate the correlation strength or sensitivity of the thermal ignition time for each of the uncertain input parameters. Pearson's correlation coefficient is defined by Eq. (22) where μ_t is the mean or the average of the computed ignition times for the n LHS samples, μ_y is the mean of the LHS inputs for the uncertain variable y, σ_t is the standard deviation of the calculated ignition times, and σ_y is the standard deviation of the LHS inputs for the uncertain variable y. Table

$$r = \frac{\frac{1}{n-1}\sum_{i=1}^{n}\left(t_i - \mu_t\right)\left(y_i - \mu_y\right)}{\sigma_t \times \sigma_y} \tag{22}$$

6 shows the uncertainty multipliers used for this LHS sampling study. Twenty ignition kinetics parameters were considered for this LHS study. All the uncertainty values were assumed to be uniformly distributed over the given range. Figure 20 of reference [1] shows that the binder migration in fully pressed PBX 9501 has a significant influence on the thermal ignition time and temperatures. The binder migration correlation given in Table 4 accounts for this migration. Previous simulations of the LSAC experiments [10] were carried out using the SITI binder migration correlation: $(1.63\text{-}0.00073\times\rho_{bo})\times0.025$. This correlation is likely to be good for geometries similar to SITI. Since the geometries of the LSAC (concentric cylinders) and the SITI (1" diameter by 1" tall cylinders) experiments are different, the binder migration is different. For this reason, the uncertainty ranges for $U_{\omega\text{BDNPA/F}}$ and $U_{\omega\text{Estane}}$ were calculated as functions of the initial bulk density, ρ_{bo}, in the binder migration correlation equation: $(1.63\text{-}0.00073\times\rho_{bo})\times0.025$. The initial bulk density , ρ_{bo}, in this equation was varied using an uncertainty multiplier of 1 ± 0.05.

The first LHS sampling study was done on the LSAC shot 1. Table 7 shows the results that include the Pearson's correlation coefficient for the ignition time. The uncertainty in the initial mass fraction of the BDNPA/F had the highest correlation with a value of 0.914. This correlation is positive, which implies that the ignition time increases when the uncertainty multiplyer of the initial bulk density in the SITI binder correlation equation increases. Since the uncertainty range for the initial mass fraction of BDNPA/F is being considered as a function of the form: $(1.63\text{-}0.00073\times\rho_{bo})\times0.025$ where the uncertainty random multiplyer multiplied ρ_{bo}, when the initial mass fraction of the BDNPA/N increases, the time to thermal ignition decreases because the SITI binder migration correlation produces an initial BDNPA/N mass fraction that decreses monotonically with an increasing initial bulk density. Figure 8 plots the ignition time against the intial BDNPA/N mass fraction produced by the LHS.

Table 6. Uncertainty multypliers for 20 ignition kinetics parameters.

Symbol	Name	Uncertainty Multyplier
U_{β_V}	Volumetric expansion	1±0.03
U_{C_b}	Bulk Specific Heat	1±0.05
$U_{\text{latent, }\beta\text{-}\delta}$	Latent Enthalpy ($\beta-\delta$)	1±0.05
$U_{\text{latent, melt}}$	Latent Enthalpy (HMX melt)	1±0.05
U_{khi}	High temperature conductivity	1±0.05
U_{klo}	Low temperature conductivity	1±0.05
U_{r_1}	Reaction 1	1±0.05
U_{r_2}	Reaction 2	1±0.05
U_{r_3}	Reaction 3	1±0.05
U_{r_4}	Reaction 4	1±0.05
U_{r_5}	Reaction 5	1±0.05
$U_{\rho_{\text{bo}}}$	Initial Bulk density	1±0.02
$U_{T\,\beta\text{-}\delta}$	$\beta-\delta$ phase change temperature	1±0.005
$U_{T\text{melt}}$	HMX melt temperature	1±0.005
U_{Ullage}	Free gas volume	1±0.005
$U_{\omega\text{BDNPA/F}}$	BDNPA/F initial mass fraction[a]	–
$U_{\omega\text{Estane}}$	Estane® initial mass fraction[b]	–
$U_{\text{H}_2\text{O}_a}$	Mass fraction of adsorbed water	1±0.10
$U_{\Sigma x\text{ihi}}$	BKWS covolume factor	1±0.05
U_{ζ}	Melt rate acceleration factor	1±0.05

[a,b]Uncertainty range was calculated as a function of the binder migration correlation, $(1.63-0.00073\times\rho_{bo})\times0.025$, by varying the initial bulk density ρ_{bo} within an uncertainty range multiplyier of 1±0.05.

Table 7. Uncertainty multipliers and correlation coefficients for LSAC experiment shot 1 The most correlated parameters are associated with the uncertainty multipyers $U_{\omega\mathrm{BDNPA/F}}$, $U_{\rho_{\mathrm{bo}}}$, U_{r_2}, and U_{r_5}.

Symbol	Name	Uncertainty Multyplier	r^c	r^2
U_{β_V}	Volumetric expansion	1±0.03	-0.059	0.003
U_{C_b}	Bulk Specific Heat	1±0.05	0.127	0.016
$U_{\mathrm{latent},\,\beta\text{-}\delta}$	Latent Enthalpy ($\beta-\delta$)	1±0.05	-0.025	0.001
$U_{\mathrm{latent,\,melt}}$	Latent Enthalpy (HMX melt)	1±0.05	-0.021	0.000
U_{khi}	High temperature conductivity	1±0.05	-0.041	0.002
U_{klo}	Low temperature conductivity	1±0.05	-0.049	0.002
U_{r_1}	Reaction 1	1±0.05	-0.038	0.001
U_{r_2}	Reaction 2	1±0.05	**-0.239**	**0.057**
U_{r_3}	Reaction 3	1±0.05	-0.046	0.002
U_{r_4}	Reaction 4	1±0.05	-0.094	0.009
U_{r_5}	Reaction 5	1±0.05	**-0.202**	**0.041**
$U_{\rho_{\mathrm{bo}}}$	Initial Bulk density	1±0.02	**0.308**	**0.095**
$U_{T\,\beta\text{-}\delta}$	$\beta-\delta$ phase change temperature	1±0.005	-0.068	0.005
$U_{T\mathrm{melt}}$	HMX melt temperature	1±0.005	-0.109	0.012
U_{Ullage}	Free gas volume	1±0.005	-0.027	0.001
$U_{\omega\mathrm{BDNPA/F}}$	BDNPA/F initial mass fraction[a]	–	**0.914**	**0.835**
$U_{\omega\mathrm{Estane}}$	Estane® initial mass fraction[b]	–	-0.128	0.016
$U_{\mathrm{H_2O_a}}$	Mass fraction of adsorbed water	1±0.10	0.143	0.020
$U_{\Sigma x\mathrm{ihi}}$	BKWS covolume factor	1±0.05	-0.121	0.015
U_{ζ}	Melt rate acceleration factor	1±0.05	-0.101	0.010

[a,b]Uncertainty range was calculated as a function of the binder migration correlation, $(1.63-0.00073\times\rho_{\mathrm{bo}})\times0.025$, by varying the initial bulk density ρ_{bo} within an uncertainty random multiplyier of 1±0.05.
[c]This is Pearson's correlation coefficient.

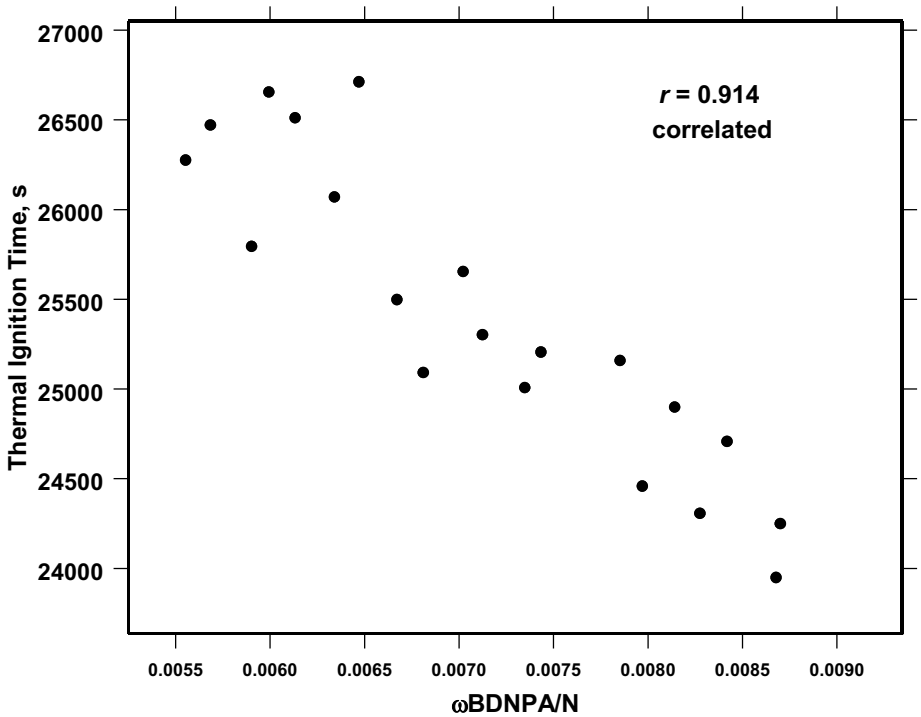

Figure 8. Thermal ignition from LHS study for LSAC shot 1 against the initial mass fraction of BDNPA/N.

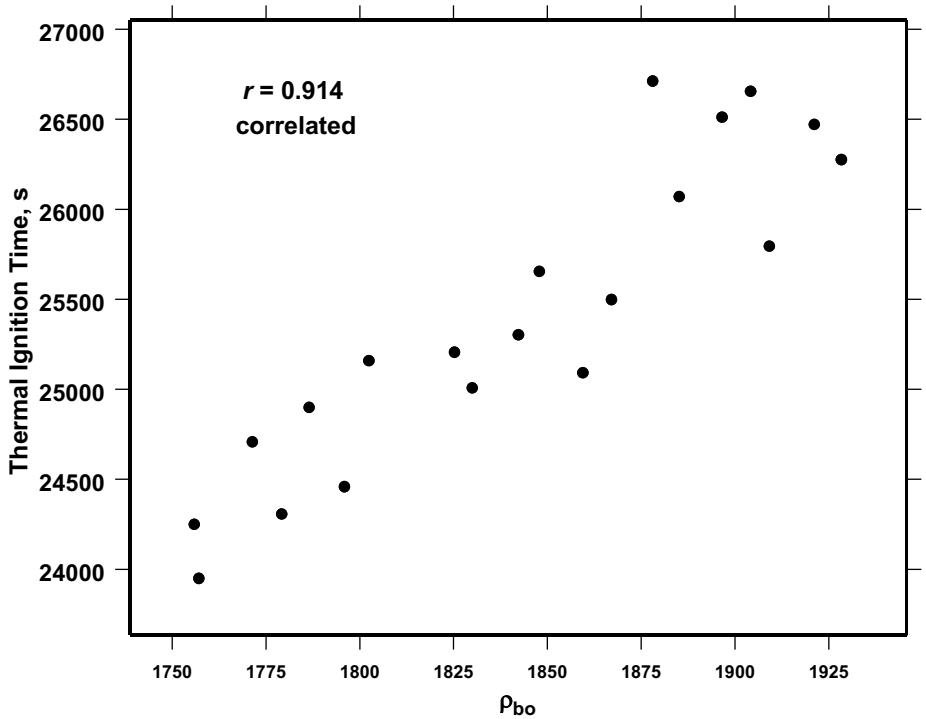

Figure 9. Thermal ignition from LHS study for LSAC shot 1 against the initial bulk density random variation considered in the binder migration correlation.

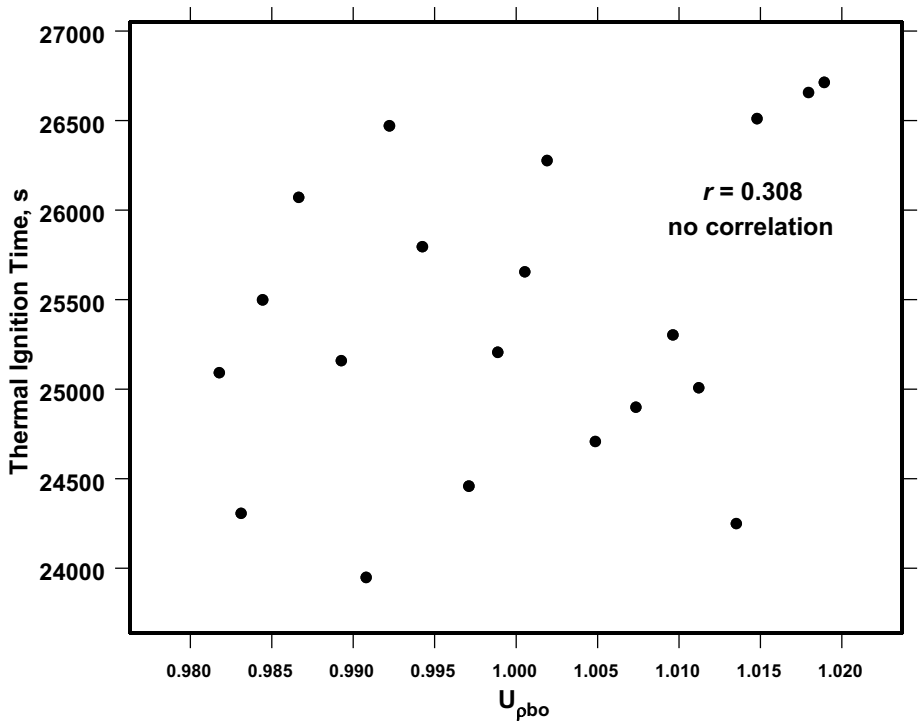

Figure 10. Thermal ignition from LHS study for LSAC shot 1 against the initial bulk density uncertainty multiplier.

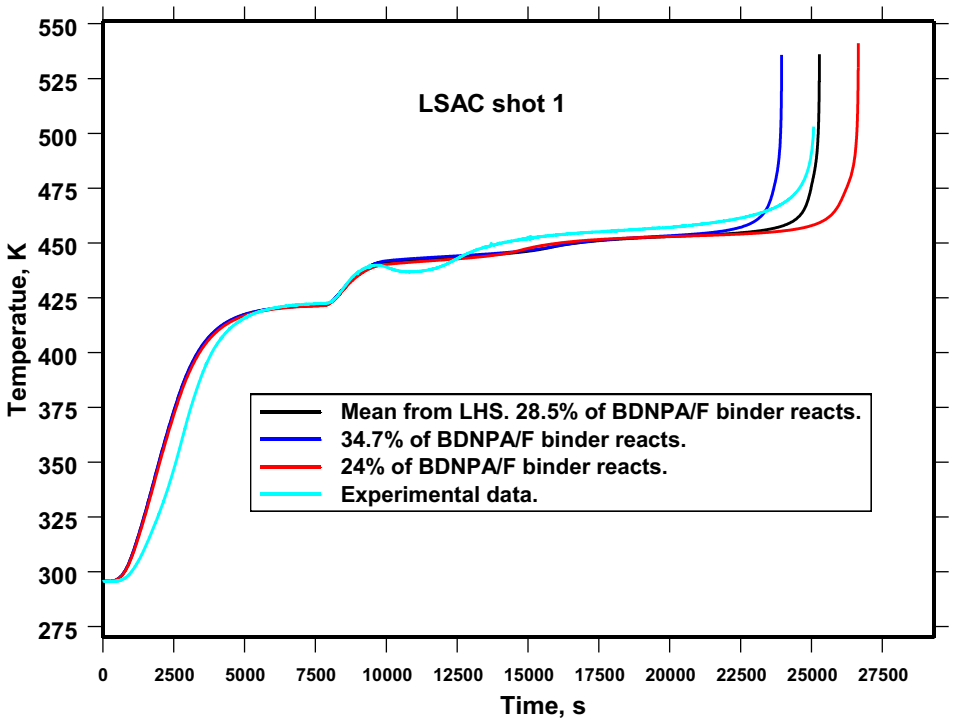

Figure 11. Upper and lower bounds, and mean from the LHS simulations of LSAC shot 1. Thermocople that measured ignition is also shown.

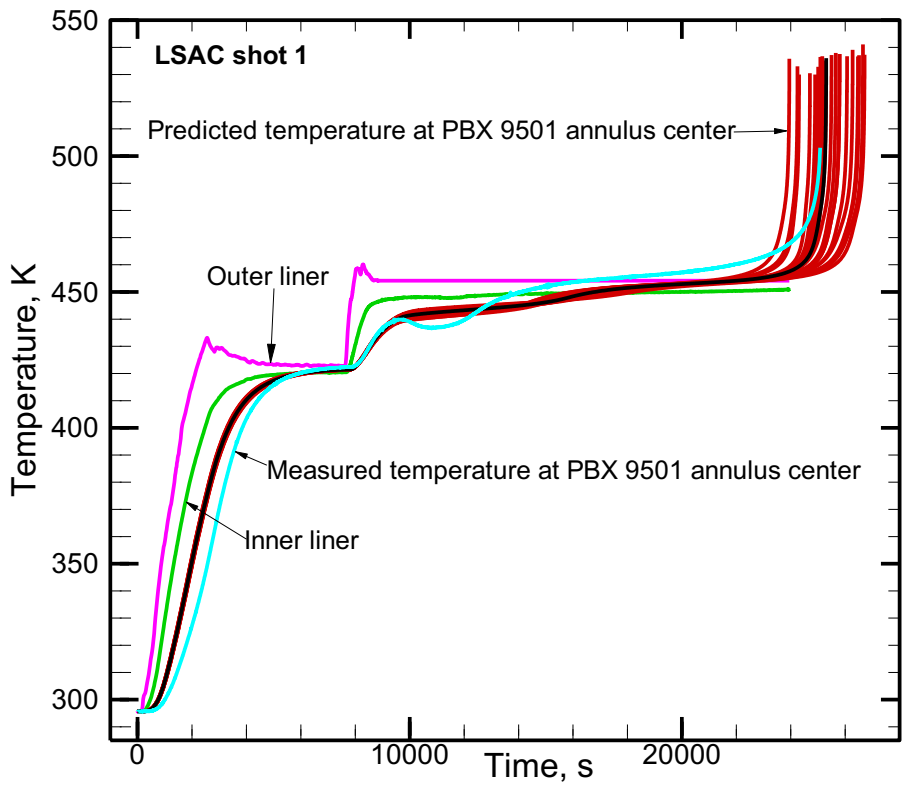

Figure 12. Simulations of 20 LHS samples using LSAC experiment shot 1.

Figure 9 plots the thermal ignition time against the random initial bulk density produced by the uncertainty multiplyer in the binder migration correlation. Note from Fig. 9 that as the initial bulk density in the binder migration correlation increases, the thermal ignition time also increases which is consistent with the sign of the correlation coefficient of +0.914. Figure 10 shows the random variation of the thermal ignition time with respect to the uncertainty multiplier of the initial bulk density, $U_{\rho_{bo}}$. This plot shows no correlation for $U_{\rho_{bo}}$. Figure 11 shows a plot of the lowest ignition time, highest ignition time, and the LHS mean ignition time from the LHS simulations of LSAC shot 1. Note from Fig. 11 that the case when 34.7% of the BDNPA/F (initial ωBDNPA/F = 0.00868) binder reacts corresponds with the lower bound of the thermal ignition time. Also, Fig. 11 shows that the case when 24% of the BDNPA/F binder (initial ωBDNPA/F = 0.005996) reacts corresponds with the upper bound of the thermal ignition time. The mean of the LHS simulations for shot 1 corresponds with the case when 28.5% of the BDNPA/F binder (initial ωBDNPA/F = 0.007128) reacts. Figure 12 shows the temperature results from the LHS simulations of LSAC experiment shot 1. The black curve represents the mean of the LHS simulations.

The second LHS sampling study was done on the LSAC shot 2. Table 8 shows the results that include the Pearson's correlation coefficient for the ignition time. The uncertainty in the initial mass fraction of the BDNPA/F had the highest correlation with a value of 0.917. This correlation is positive, which implies that the ignition time increases when the uncertainty multiplyer of the initial bulk density in the SITI binder correlation equation increases. Figure 13 plots the ignition time against the initial BDNPA/F mass

Table 8. Uncertainty multipliers and correlation coefficients for LSAC experiment shot 2 The most correlated parameters are associated with the uncertainty multipyers $U_{\omega\mathrm{BDNPA/F}}$, $U_{\rho_{\mathrm{bo}}}$, U_{r_2}, U_{r_5} and $U_{\omega\mathrm{Estane}}$.

Symbol	Name	Uncertainty Multyplier	r^c	r^2
U_{β_V}	Volumetric expansion	1±0.03	-0.070	0.005
U_{C_b}	Bulk Specific Heat	1±0.05	0.134	0.018
$U_{\mathrm{latent},\,\beta\text{-}\delta}$	Latent Enthalpy ($\beta-\delta$)	1±0.05	-0.018	0.000
$U_{\mathrm{latent,\,melt}}$	Latent Enthalpy (HMX melt)	1±0.05	-0.016	0.000
U_{khi}	High temperature conductivity	1±0.05	-0.024	0.001
U_{klo}	Low temperature conductivity	1±0.05	-0.013	0.000
U_{r_1}	Reaction 1	1±0.05	-0.044	0.002
U_{r_2}	Reaction 2	1±0.05	**-0.230**	**0.053**
U_{r_3}	Reaction 3	1±0.05	0.017	0.000
U_{r_4}	Reaction 4	1±0.05	-0.103	0.011
U_{r_5}	Reaction 5	1±0.05	**-0.207**	**0.043**
$U_{\rho_{\mathrm{bo}}}$	Initial Bulk density	1±0.02	**0.250**	**0.062**
$U_{T\,\beta\text{-}\delta}$	$\beta-\delta$ phase change temperature	1±0.005	0.026	0.001
$U_{T\mathrm{melt}}$	HMX melt temperature	1±0.005	-0.130	0.017
U_{Ullage}	Free gas volume	1±0.005	-0.011	0.000
$U_{\omega\mathrm{BDNPA/F}}$	BDNPA/F initial mass fraction[a]	–	**0.917**	**0.842**
$U_{\omega\mathrm{Estane}}$	Estane® initial mass fraction[b]	–	**-0.204**	**0.042**
$U_{\mathrm{H_2O_a}}$	Mass fraction of adsorbed water	1±0.10	0.158	0.025
$U_{\Sigma x\mathrm{hi}}$	BKWS covolume factor	1±0.05	-0.111	0.012
U_{ζ}	Melt rate acceleration factor	1±0.05	-0.079	0.006

[a,b]Uncertainty range was calculated as a function of the binder migration correlation, $(1.63-0.00073\times\rho_{\mathrm{bo}})\times0.025$, by varying the initial bulk density ρ_{bo} within an uncertainty random multiplyier of 1±0.05.
[c]This is Pearson's correlation coefficient.

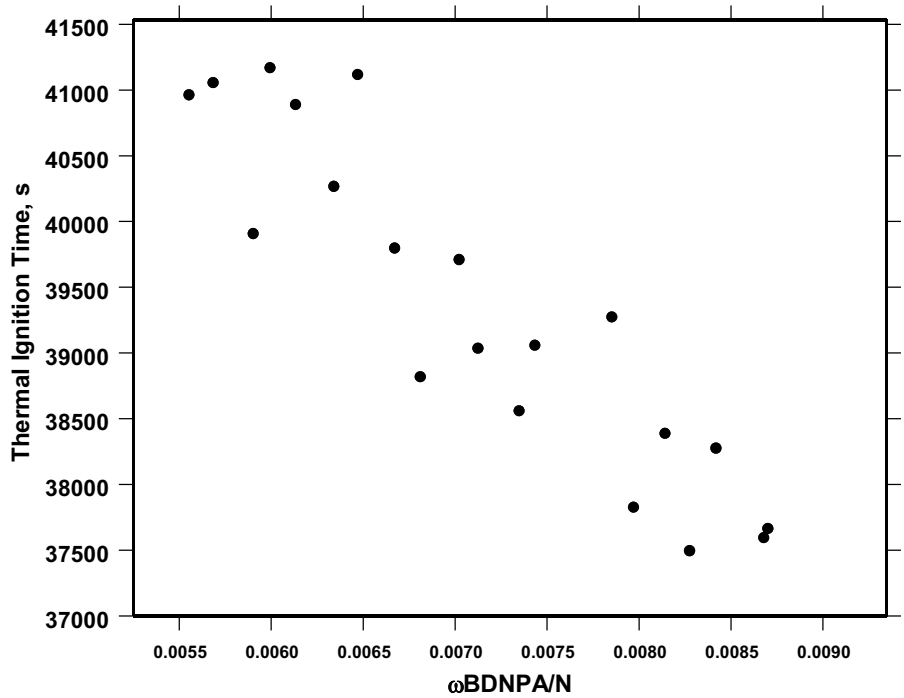

Figure 13. Thermal ignition from LHS study for LSAC shot 2 against the initial mass fraction of BDNPA/N.

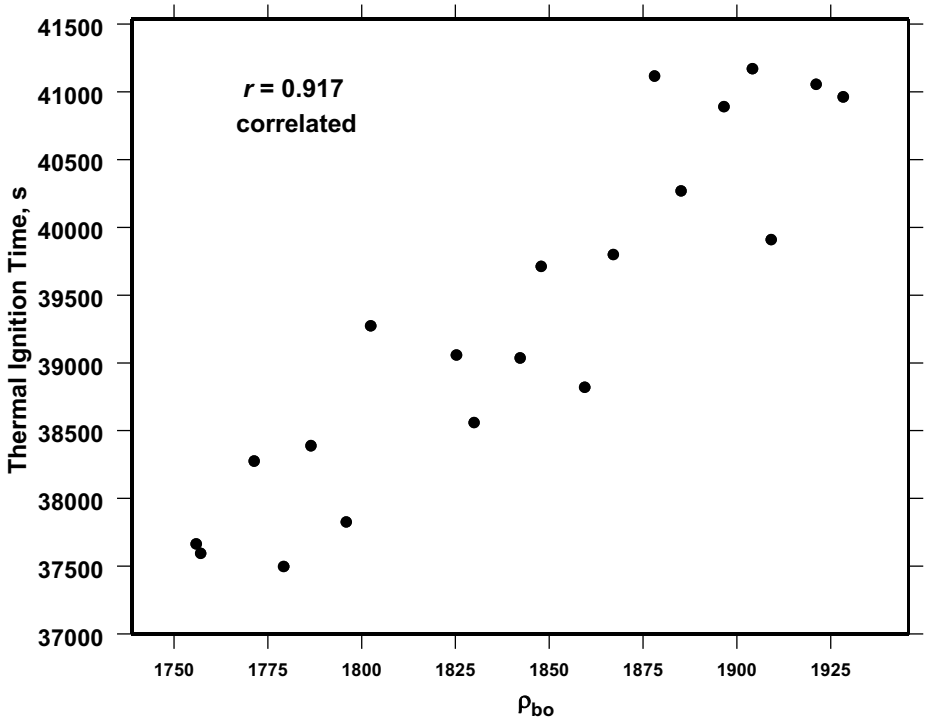

Figure 14. Thermal ignition from LHS study for LSAC shot 2 against the initial bulk density random variation considered in the binder migration correlation.

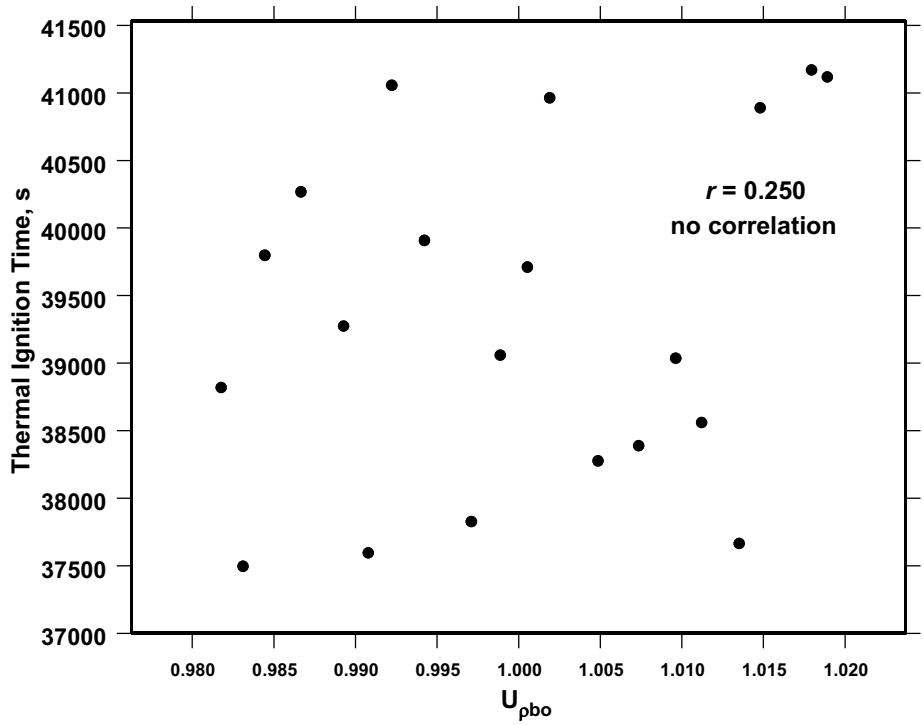

Figure 15. Thermal ignition from LHS study for LSAC shot 2 against the initial bulk density uncertainty multiplier.

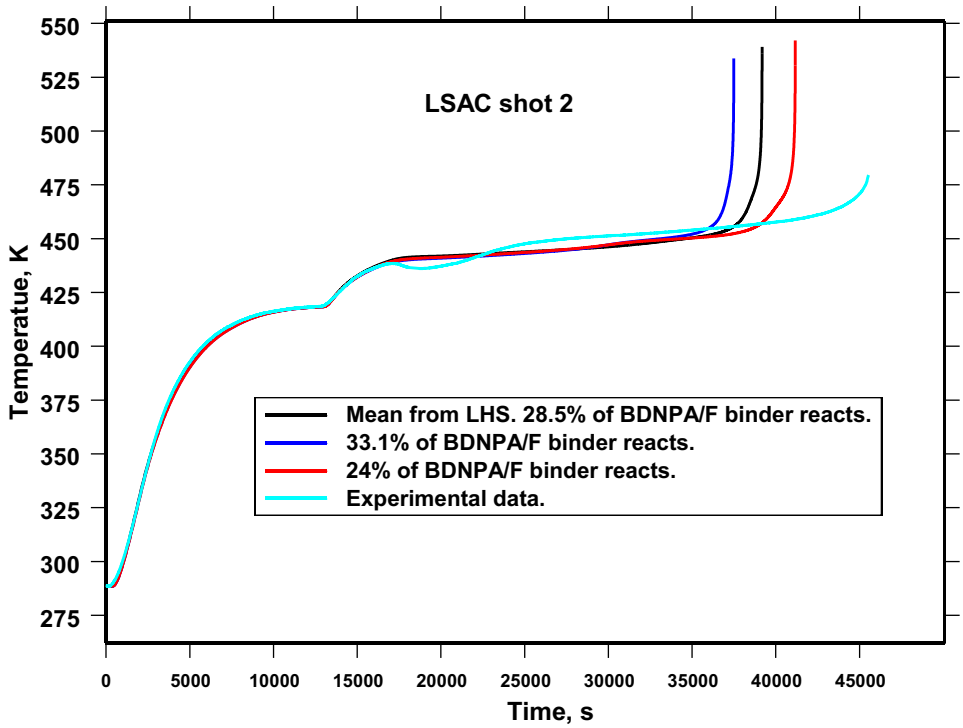

Figure 16. Upper and lower bounds, and mean from the LHS simulations of LSAC shot 2. Thermocople that measured ignition is also shown.

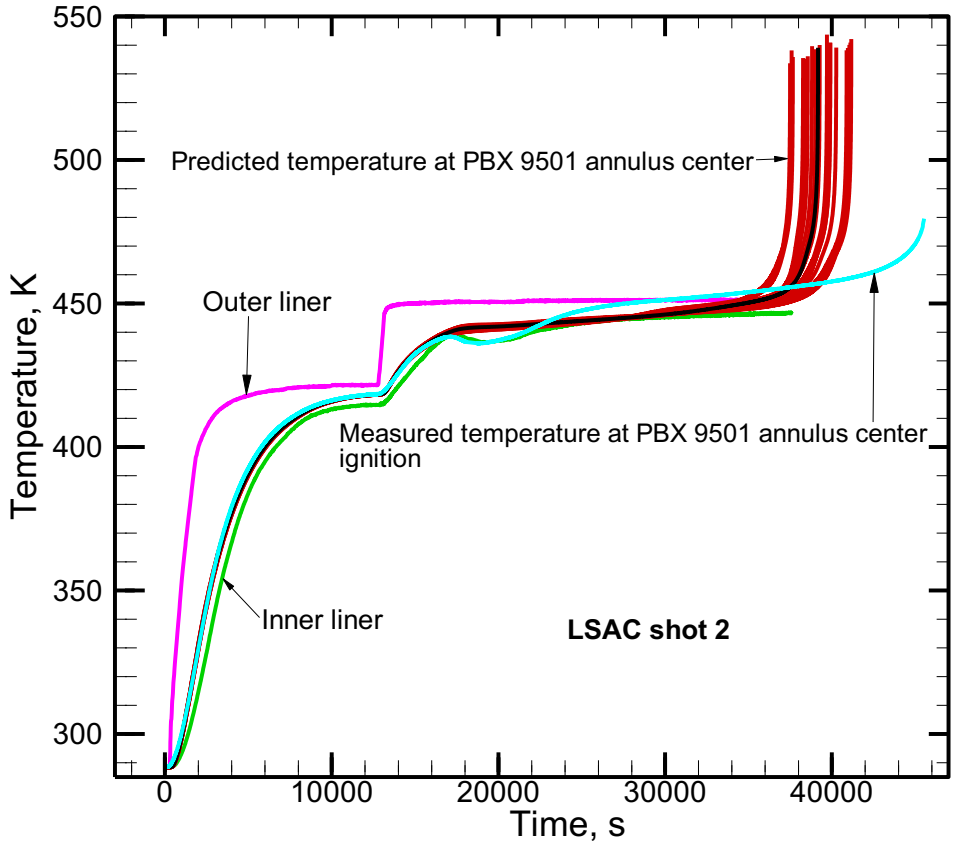

Figure 17. Simulations of 20 LHS samples using LSAC experiment shot 2.

fraction produced by the LHS simulations of LSAC shot 2. Figure 14 plots the thermal ignition time against the random initial bulk density produced by the uncertainty multiplyer in the binder migration correlation. Note from Fig. 14 that as the initial bulk density contained in the binder migration correlation increases, the thermal ignition time also increases which is consistent with the sign of the correlation coefficient of +0.917. Figure 15 shows the random variation of the thermal ignition time with respect to the uncertainty multiplier of the initial bulk density, $U_{\rho_{bo}}$. This plot shows no correlation for $U_{\rho_{bo}}$. Figure 16 shows a plot of the lowest ignition time, highest ignition time, and the LHS mean ignition time from the LHS simulations of LSAC shot 2. Note from Fig. 16 that the case when 33.1% of the BDNPA/F (initial $\omega\text{BDNPA/F} = 0.008277$) binder reacts corresponds with the lower bound of the thermal ignition time. Also, Fig. 16 shows that the case when 24% of the BDNPA/F binder (initial $\omega\text{BDNPA/F} = 0.005996$) reacts corresponds with the upper bound of the thermal ignition time. The mean of the LHS simulations for shot 2 corresponds with the case when 28.5% of the BDNPA/F binder (initial $\omega\text{BDNPA/F} = 0.007128$) reacts in Fig. 16. Figure 17 shows the temperature results from the LHS simulations of LSAC experiment shot 2. The black curve represents the mean of the LHS simulations.

The third LHS sampling study was done on the LSAC shot 3. Table 9 shows the results that include the Pearson's correlation coefficient for the ignition time. The uncertainty in the initial mass fraction of the BDNPA/F had the highest correlation with a value of 0.919.

Table 9. Uncertainty multipliers and correlation coefficients for LSAC experiment shot 3 The most correlated parameters are associated with the uncertainty multipyers $U_{\omega\mathrm{BDNPA/F}}$, $U_{\rho_{\mathrm{bo}}}$, U_{r_2}, U_{r_5} and $U_{\omega\mathrm{Estane}}$.

Symbol	Name	Uncertainty Multyplier	r^c	r^2
U_{β_V}	Volumetric expansion	1±0.03	-0.067	0.004
U_{C_b}	Bulk Specific Heat	1±0.05	0.133	0.018
$U_{\mathrm{latent},\,\beta\text{-}\delta}$	Latent Enthalpy ($\beta-\delta$)	1±0.05	-0.0157	0.000
$U_{\mathrm{latent,\,melt}}$	Latent Enthalpy (HMX melt)	1±0.05	-0.0181	0.000
U_{khi}	High temperature conductivity	1±0.05	-0.037	0.001
U_{klo}	Low temperature conductivity	1±0.05	-0.021	0.000
U_{r_1}	Reaction 1	1±0.05	-0.041	0.002
U_{r_2}	Reaction 2	1±0.05	**-0.225**	**0.051**
U_{r_3}	Reaction 3	1±0.05	0.011	0.000
U_{r_4}	Reaction 4	1±0.05	-0.103	0.011
U_{r_5}	Reaction 5	1±0.05	**-0.200**	**0.040**
$U_{\rho_{\mathrm{bo}}}$	Initial Bulk density	1±0.02	**0.257**	**0.066**
$U_{T\,\beta\text{-}\delta}$	$\beta-\delta$ phase change temperature	1±0.005	0.022	0.000
$U_{T\mathrm{melt}}$	HMX melt temperature	1±0.005	-0.128	0.016
U_{Ullage}	Free gas volume	1±0.005	-0.0128	0.000
$U_{\omega\mathrm{BDNPA/F}}$	BDNPA/F initial mass fraction[a]	–	**0.919**	**0.845**
$U_{\omega\mathrm{Estane}}$	Estane® initial mass fraction[b]	–	**-0.191**	**0.036**
$U_{\mathrm{H_2O_a}}$	Mass fraction of adsorbed water	1±0.10	0.150	0.022
$U_{\Sigma x\mathrm{ihi}}$	BKWS covolume factor	1±0.05	-0.112	0.013
U_{ζ}	Melt rate acceleration factor	1±0.05	-0.085	0.007

[a,b]Uncertainty range was calculated as a function of the binder migration correlation, $(1.63-0.00073\times\rho_{\mathrm{bo}})\times0.025$, by varying the initial bulk density ρ_{bo} within an uncertainty random multiplyier of 1±0.05.
[c]This is Pearson's correlation coefficient.

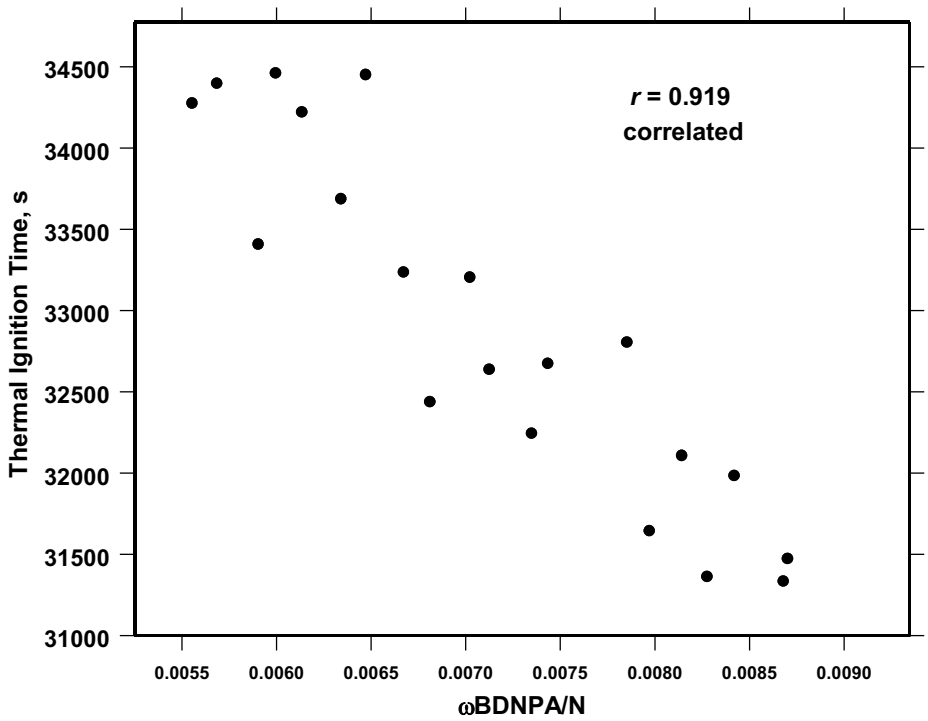

Figure 18. Thermal ignition from LHS study for LSAC shot 3 against the initial mass fraction of BDNPA/N.

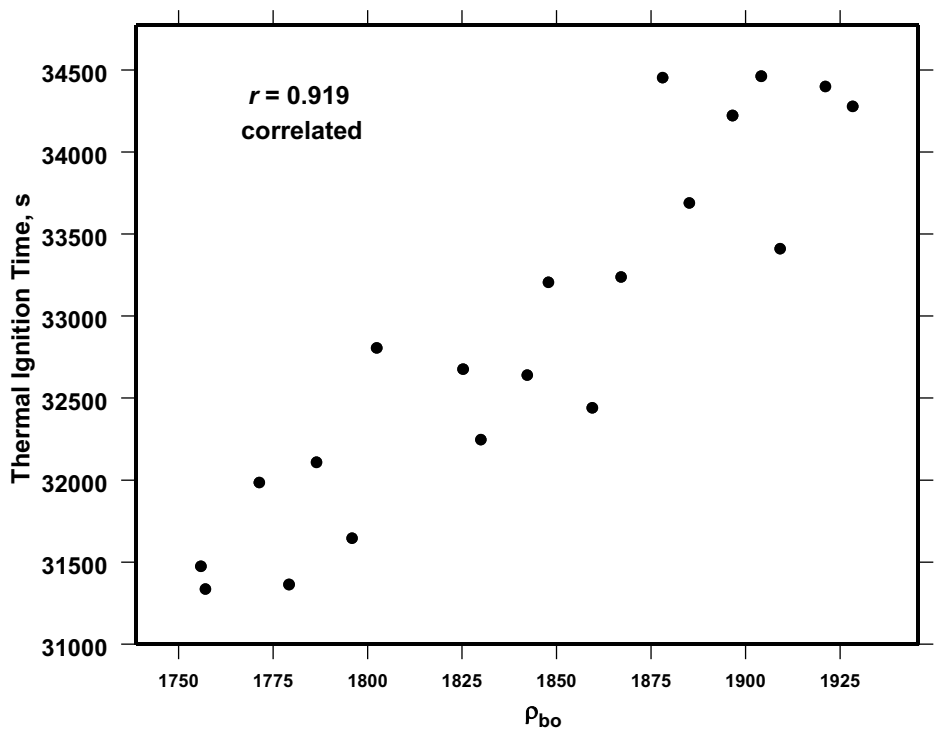

Figure 19. Thermal ignition from LHS study for LSAC shot 3 against the initial bulk density random variation considered in the binder migration correlation.

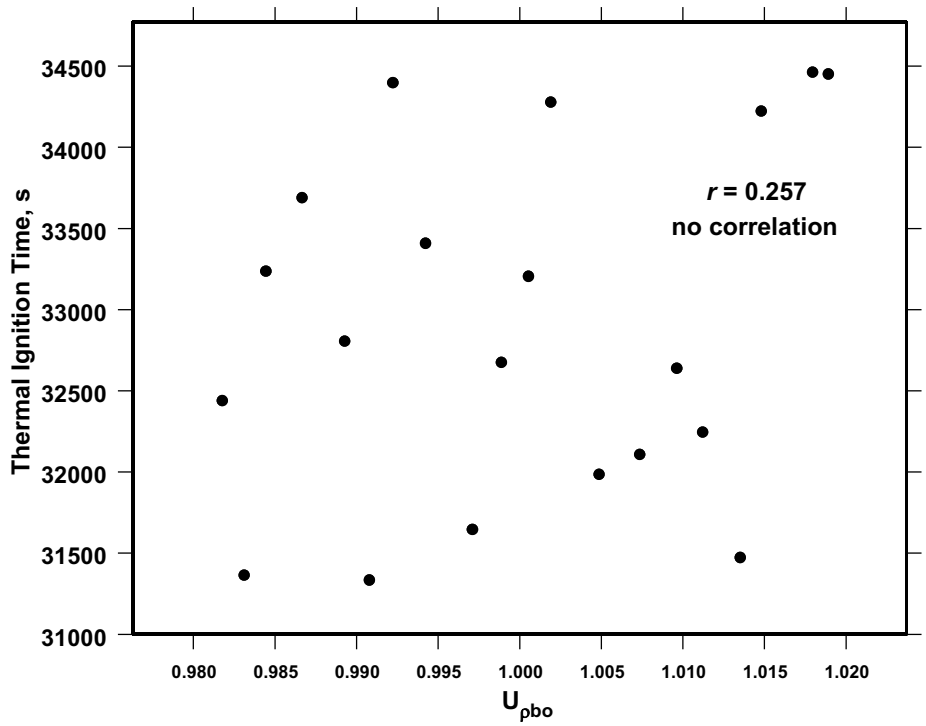

Figure 20. Thermal ignition from LHS study for LSAC shot 3 against the initial bulk density uncertainty multiplier.

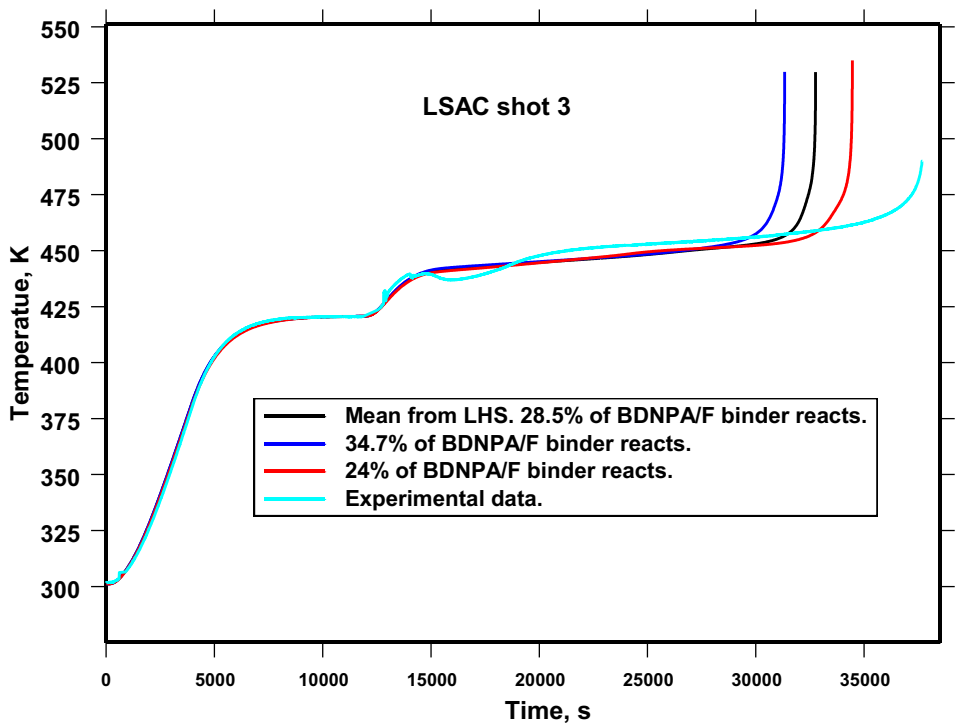

Figure 21. Upper and lower bounds, and mean from the LHS simulations of LSAC shot 3. Thermocople that measured ignition is also shown.

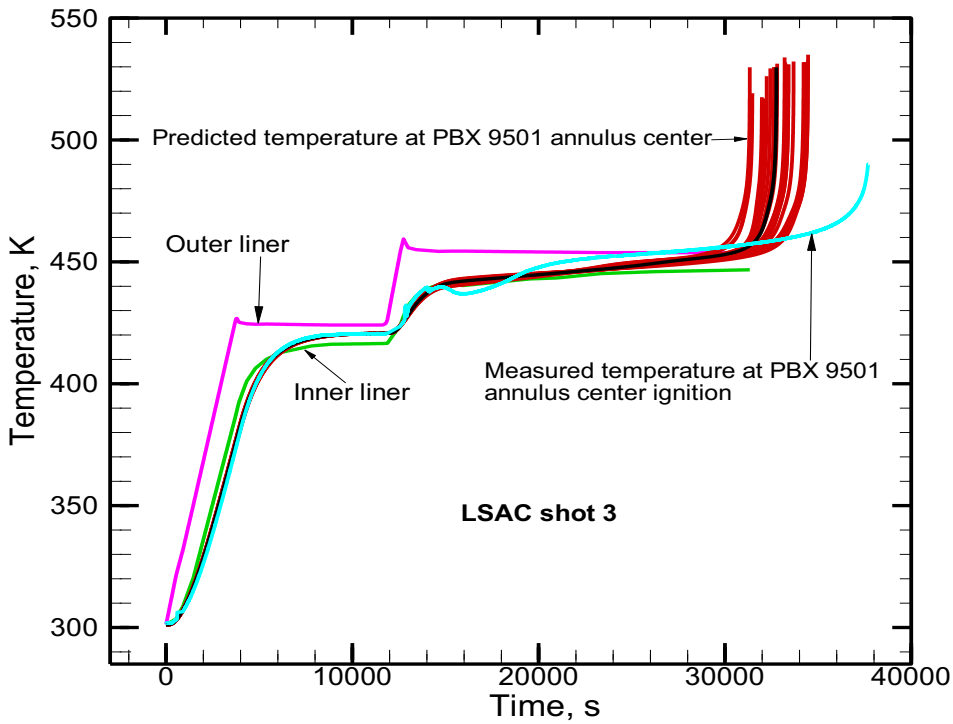

Figure 22. Simulations of 20 LHS samples using LSAC experiment shot 3.

This correlation is positive, which implies that the ignition time increases when the uncertainty multiplyer of the initial bulk density in the SITI binder correlation equation increases. Figure 18 plots the ignition time against the initial BDNPA/F mass fraction produced by the LHS simulations of LSAC shot 3. Figure 19 plots the thermal ignition time against the random initial bulk density produced by the uncertainty multiplyer in the binder migration correlation. Note from Fig. 19 that as the initial bulk density contained in the binder migration correlation increases, the thermal ignition time also increases which is consistent with the sign of the correlation coefficient of +0.919. Figure 20 shows the random variation of the thermal ignition time with respect to the uncertainty multiplier of the initial bulk density, $U_{\rho_{bo}}$. This plot shows no correlation for $U_{\rho_{bo}}$. Figure 21 shows a plot of the lowest ignition time, highest ignition time, and the LHS mean ignition time from the LHS simulations of LSAC shot 3. Note from Fig. 21 that the case when 34.7% of the BDNPA/F (initial ωBDNPA/F = 0.0086807) binder reacts corresponds with the lower bound of the thermal ignition time. Also, Fig. 21 shows that the case when 24% of the BDNPA/F binder (initial ωBDNPA/F = 0.005996) reacts corresponds with the upper bound of the thermal ignition time. The mean of the LHS simulations for shot 3 corresponds with the case when 28.5% of the BDNPA/F binder (initial ωBDNPA/F = 0.007128) reacts in Fig. 21. Figure 22 shows the temperature results from the LHS simulations of LSAC experiment shot 3. The black curve represents the mean of the LHS simulations.

The fourth LHS sampling study was done on the LSAC shot 5. Table 10 shows the results that include the Pearson's correlation coefficient for the ignition time. The uncertainty in the initial mass fraction of the BDNPA/F had the highest correlation with a value of 0.915. This correlation is positive, which implies that the ignition time increases when

Table 10. Uncertainty multipliers and correlation coefficients for LSAC experiment shot 5 The most correlated parameters are associated with the uncertainty multipyers $U_{\omega\mathrm{BDNPA/F}}$, $U_{\rho_{\mathrm{bo}}}$, U_{r_2}, U_{r_5}, $U_{\mathrm{H_2O_a}}$, and $U_{\omega\mathrm{Estane}}$.

Symbol	Name	Uncertainty Multyplier	r^c	r^2
U_{β_V}	Volumetric expansion	1±0.03	-0.061	0.004
U_{C_b}	Bulk Specific Heat	1±0.05	0.129	0.017
$U_{\mathrm{latent},\,\beta\text{-}\delta}$	Latent Enthalpy ($\beta-\delta$)	1±0.05	-0.029	0.001
$U_{\mathrm{latent,\,melt}}$	Latent Enthalpy (HMX melt)	1±0.05	-0.022	0.000
U_{khi}	High temperature conductivity	1±0.05	-0.024	0.001
U_{klo}	Low temperature conductivity	1±0.05	-0.050	0.002
U_{r_1}	Reaction 1	1±0.05	-0.040	0.002
U_{r_2}	Reaction 2	1±0.05	**-0.238**	**0.060**
U_{r_3}	Reaction 3	1±0.05	-0.040	0.002
U_{r_4}	Reaction 4	1±0.05	-0.091	0.008
U_{r_5}	Reaction 5	1±0.05	**-0.207**	**0.043**
$U_{\rho_{\mathrm{bo}}}$	Initial Bulk density	1±0.02	**0.300**	**0.090**
$U_{T\,\beta\text{-}\delta}$	$\beta-\delta$ phase change temperature	1±0.005	-0.051	0.003
$U_{T\mathrm{melt}}$	HMX melt temperature	1±0.005	0.111	0.012
U_{Ullage}	Free gas volume	1±0.005	-0.023	0.000
$U_{\omega\mathrm{BDNPA/F}}$	BDNPA/F initial mass fraction[a]	–	**0.915**	**0.838**
$U_{\omega\mathrm{Estane}}$	Estane® initial mass fraction[b]	–	**-0.129**	**0.017**
$U_{\mathrm{H_2O_a}}$	Mass fraction of adsorbed water	1±0.10	**0.143**	**0.021**
$U_{\Sigma x\mathrm{hi}}$	BKWS covolume factor	1±0.05	-0.119	0.014
U_{ζ}	Melt rate acceleration factor	1±0.05	-0.100	0.010

[a,b]Uncertainty range was calculated as a function of the binder migration correlation, $(1.63-0.00073\times\rho_{\mathrm{bo}})\times0.025$, by varying the initial bulk density ρ_{bo} within an uncertainty random multiplyier of 1±0.05.
[c]This is Pearson's correlation coefficient.

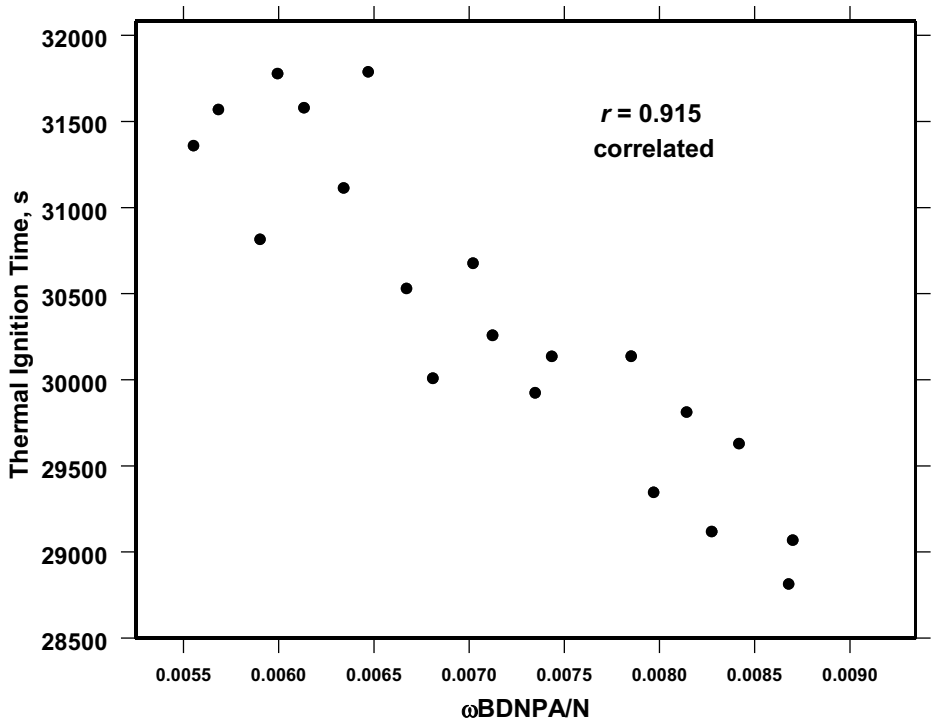

Figure 23. Thermal ignition from LHS study for LSAC shot 5 against the initial mass fraction of BDNPA/N.

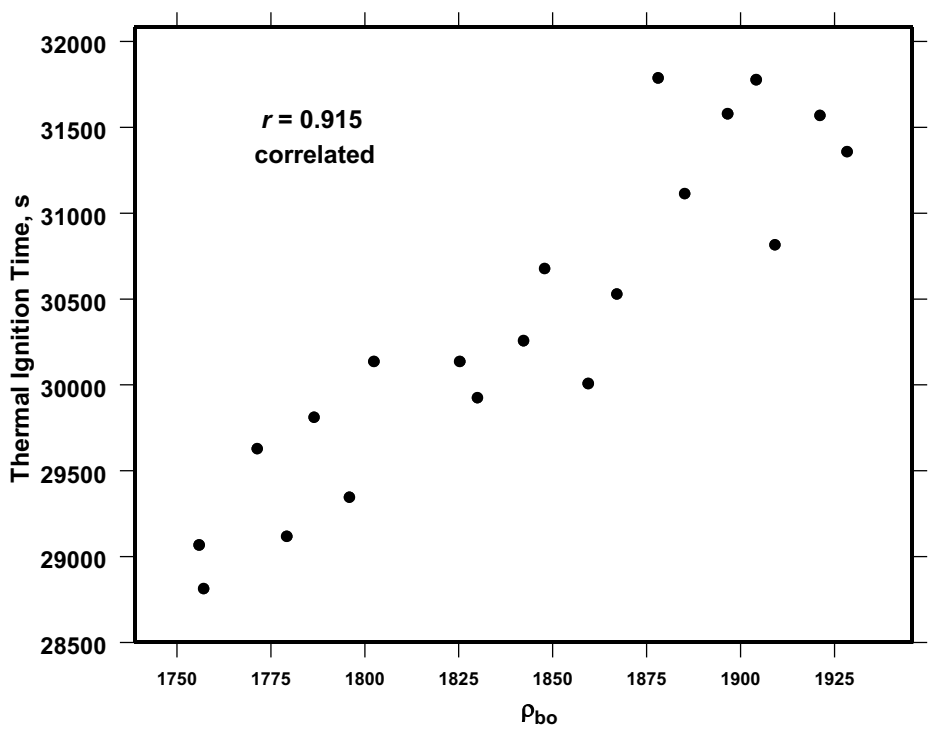

Figure 24. Thermal ignition from LHS study for LSAC shot 5 against the initial bulk density random variation considered in the binder migration correlation.

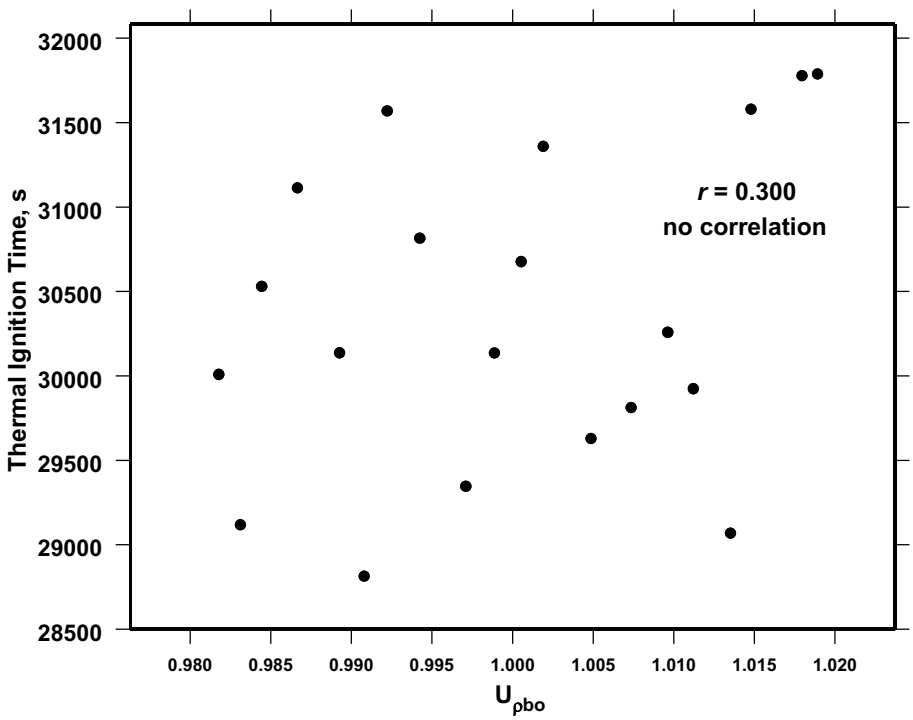

Figure 25. Thermal ignition from LHS study for LSAC shot 5 against the initial bulk density uncertainty multiplier.

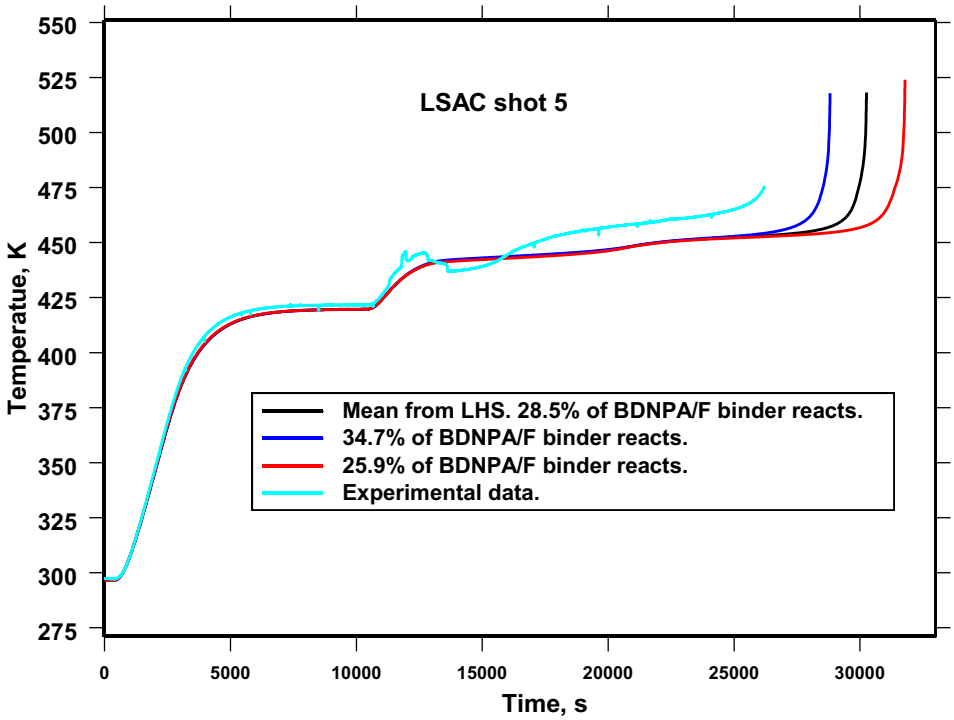

Figure 26. Upper and lower bounds, and mean from the LHS simulations of LSAC shot 5. Thermocople that measured ignition is also shown.

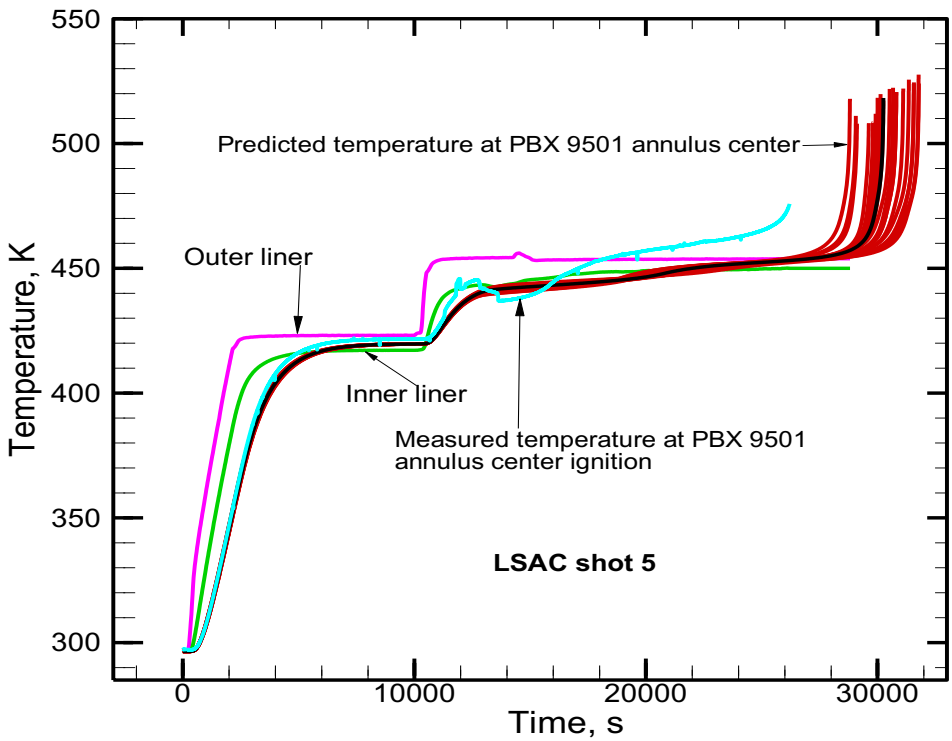

Figure 27. Simulations of 20 LHS samples using LSAC experiment shot 5.

the uncertainty multiplyer of the initial bulk density in the SITI binder correlation equation increases. Figure 23 plots the ignition time against the initial BDNPA/F mass fraction produced by the LHS simulations of LSAC shot 5. Figure 24 plots the thermal ignition time against the random initial bulk density produced by the uncertainty multiplyer contained in the binder migration correlation. Note from Fig. 24 that as the initial bulk density contained in the binder migration correlation increases, the thermal ignition time also increases which is consistent with the sign of the correlation coefficient of +0.919. Figure 25 shows the random variation of the thermal ignition time with respect to the uncertainty multiplier of the initial bulk density, $U_{\rho_{bo}}$. This plot shows no correlation for $U_{\rho_{bo}}$. Figure 26 shows a plot of the lowest ignition time, highest ignition time, and the LHS mean ignition time from the LHS simulations of LSAC shot 5. Note from Fig. 26 that the case when 34.7% of the BDNPA/F (initial ωBDNPA/F = 0.0086807) binder reacts corresponds with the lower bound of the thermal ignition time. Also, Fig. 21 shows that the case when 25.9% of the BDNPA/F binder (initial ωBDNPA/F = 006473) reacts corresponds with the upper bound of the thermal ignition time. The mean of the LHS simulations for shot 5 corresponds with the case when 28.5% of the BDNPA/F binder (initial ωBDNPA/F = 0.007128) reacts in Fig. 21. Figure 27 shows the temperature results from the LHS simulations of LSAC experiment shot 5. The black curve represents the mean of the LHS simulations.

The fifth LHS sampling study was done on the LSAC shot 6. Table 11 shows the results that include the Pearson's correlation coefficient for the ignition time. The uncertainty in the initial mass fraction of the BDNPA/F had the highest correlation with a value of 0.912. This correlation is positive, which implies that the ignition time increases when the uncertainty multiplyer of the initial bulk density in the SITI binder correlation equation increases. Figure 28

Table 11. Uncertainty multipliers and correlation coefficients for LSAC experiment shot 6. The most correlated parameters are associated with the uncertainty multipyers $U_{\omega\text{BDNPA/F}}$, $U_{\rho_{\text{bo}}}$, U_{r_2}, U_{r_5}, $U_{\text{H}_2\text{O}_\text{a}}$, and $U_{\omega\text{Estane}}$.

Symbol	Name	Uncertainty Multyplier	r^c	r^2
U_{β_V}	Volumetric expansion	1±0.03	-0.060	0.004
U_{C_b}	Bulk Specific Heat	1±0.05	0.130	0.017
$U_{\text{latent, }\beta\text{-}\delta}$	Latent Enthalpy ($\beta-\delta$)	1±0.05	-0.022	0.000
$U_{\text{latent, melt}}$	Latent Enthalpy (HMX melt)	1±0.05	-0.019	0.000
U_{khi}	High temperature conductivity	1±0.05	-0.037	0.001
U_{klo}	Low temperature conductivity	1±0.05	-0.052	0.003
U_{r_1}	Reaction 1	1±0.05	-0.038	0.001
U_{r_2}	Reaction 2	1±0.05	**-0.235**	**0.055**
U_{r_3}	Reaction 3	1±0.05	-0.045	0.002
U_{r_4}	Reaction 4	1±0.05	-0.092	0.008
U_{r_5}	Reaction 5	1±0.05	**-0.218**	**0.047**
$U_{\rho_{\text{bo}}}$	Initial Bulk density	1±0.02	**0.303**	**0.092**
$U_{T\,\beta\text{-}\delta}$	$\beta-\delta$ phase change temperature	1±0.005	-0.069	0.005
$U_{T\text{melt}}$	HMX melt temperature	1±0.005	-0.106	0.011
U_{Ullage}	Free gas volume	1±0.005	-0.030	0.001
$U_{\omega\text{BDNPA/F}}$	BDNPA/F initial mass fraction[a]	–	**0.912**	**0.833**
$U_{\omega\text{Estane}}$	Estane® initial mass fraction[b]	–	**-0.130**	**0.017**
$U_{\text{H}_2\text{O}_\text{a}}$	Mass fraction of adsorbed water	1±0.10	**0.141**	**0.020**
$U_{\Sigma x\text{hi}}$	BKWS covolume factor	1±0.05	-0.121	0.015
U_{ζ}	Melt rate acceleration factor	1±0.05	-0.101	0.010

[a,b]Uncertainty range was calculated as a function of the binder migration correlation, $(1.63-0.00073\times\rho_{\text{bo}})\times0.025$, by varying the initial bulk density ρ_{bo} within an uncertainty random multiplyier of 1±0.05.
[c]This is Pearson's correlation coefficient.

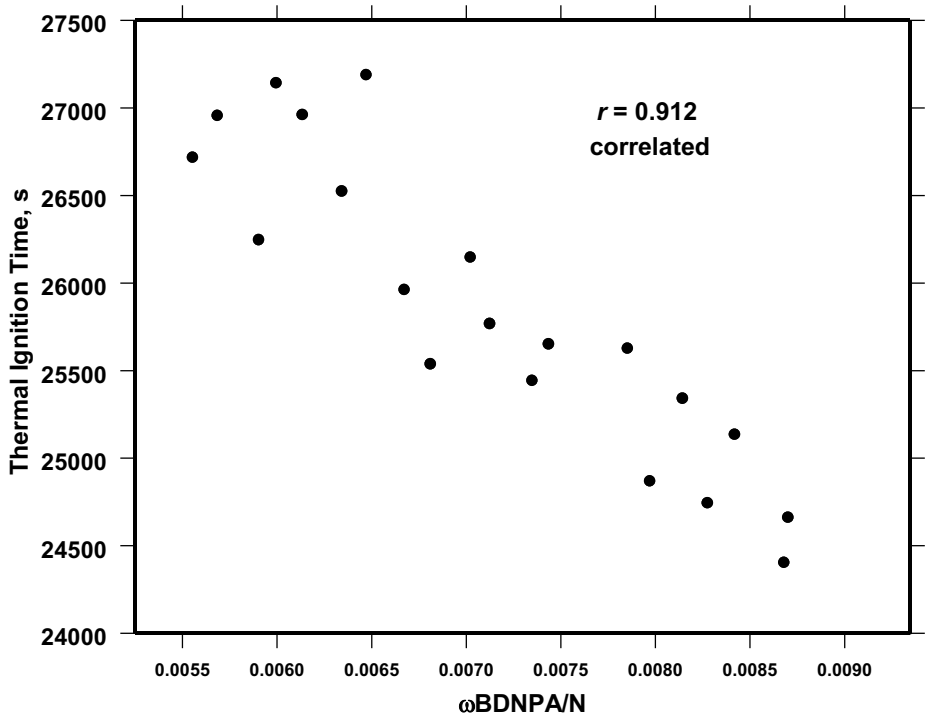

Figure 28. Thermal ignition from LHS study for LSAC shot 6 against the initial mass fraction of BDNPA/N.

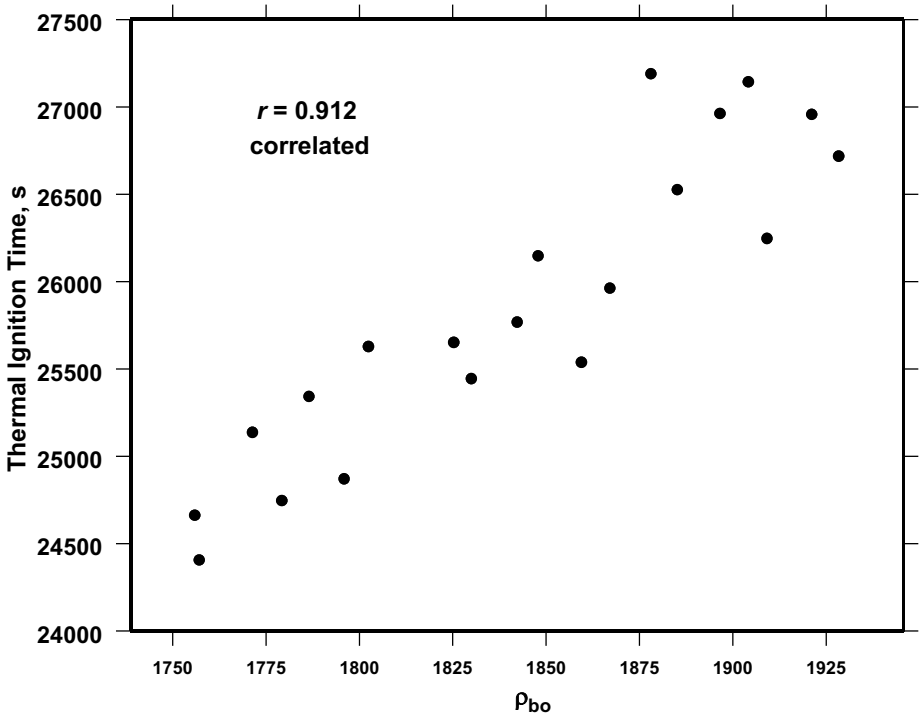

Figure 29. Thermal ignition from LHS study for LSAC shot 6 against the initial bulk density random variation considered in the binder migration correlation.

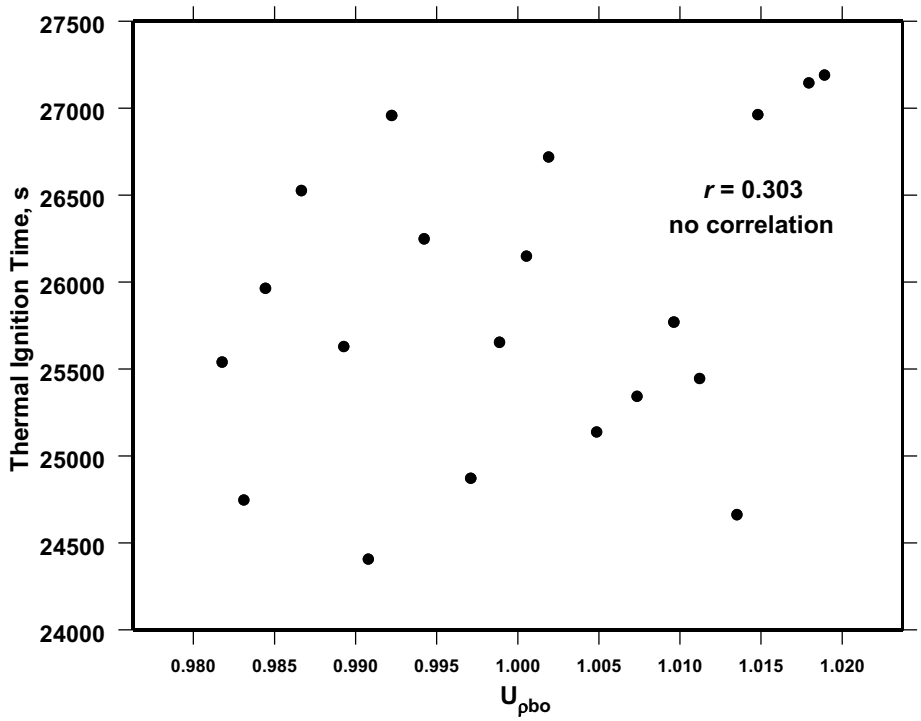

Figure 30. Thermal ignition from LHS study for LSAC shot 6 against the Initial bulk density uncertainty multiplier.

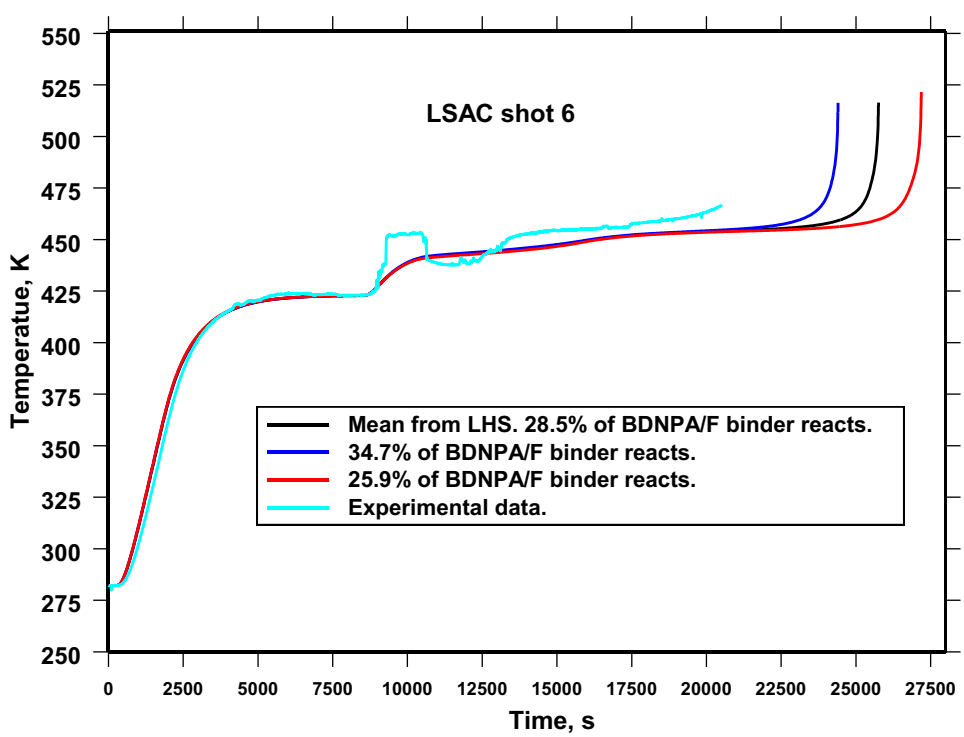

Figure 31. Upper and lower bounds, and mean from the LHS simulations of LSAC shot 6. Thermocople that measured ignition is also shown.

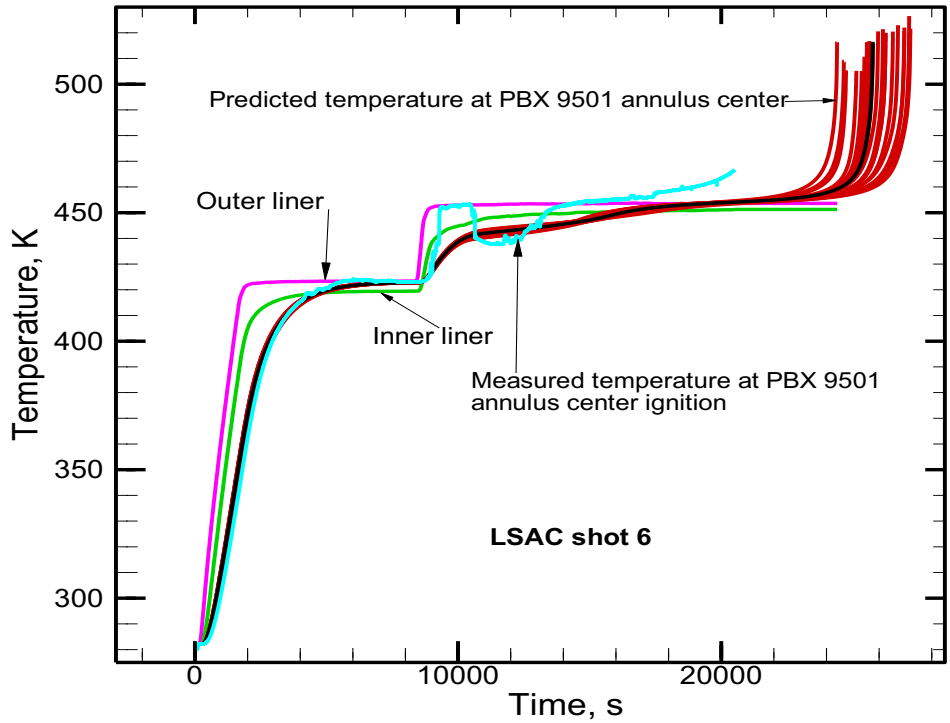

Figure 32. Simulations of 20 LHS samples using LSAC experiment shot 6.

plots the ignition time against the initial BDNPA/F mass fraction produced by the LHS simulations of LSAC shot 6. Figure 29 plots the thermal ignition time against the random initial bulk density produced by the uncertainty multiplyer contained in the binder migration correlation. Note from Fig. 29 that as the initial bulk density contained in the binder migration correlation increases, the thermal ignition time also increases which is consistent with the sign of the correlation coefficient of +0.912. Figure 30 shows the random variation of the thermal ignition time with respect to the uncertainty multiplier of the initial bulk density, $U_{\rho_{bo}}$. This plot shows no correlation for $U_{\rho_{bo}}$. Figure 31 shows a plot of the lowest ignition time, highest ignition time, and the LHS mean ignition time from the LHS simulations of LSAC shot 6. Note from Fig. 31 that the case when 34.7% of the BDNPA/F (initial ωBDNPA/F = 0.0086807) binder reacts corresponds with the lower bound of the thermal ignition time. Also, Fig. 31 shows that the case when 25.9% of the BDNPA/F binder (initial ωBDNPA/F =0.006473) reacts corresponds with the upper bound of the thermal ignition time. The mean of the LHS simulations for shot 6 corresponds with the case when 28.5% of the BDNPA/F binder (initial ωBDNPA/F = 0.007128) reacts in Fig. 31. Figure 32 shows the temperature results from the LHS simulations of LSAC experiment shot 6. The black curve represents the mean of the LHS simulations.

The sixth LHS sampling study was done on the LSAC shot 7. Table 12 shows the results that include the Pearson's correlation coefficient for the ignition time. The uncertainty in the initial mass fraction of the BDNPA/F had the highest correlation with a value of 0.911. This correlation is positive, which implies that the ignition time increases when the uncertainty multiplyer of the initial bulk density in the SITI binder correlation equation increases. Figure 33 plots the ignition time against the initial BDNPA/F mass fraction produced by the LHS simulations of LSAC shot 7. Figure 34 plots the thermal ignition time against the random initial

Table 12. Uncertainty multipliers and correlation coefficients for LSAC experiment shot 7. The most correlated parameters are associated with the uncertainty multipyers $U_{\omega\mathrm{BDNPA/F}}$, $U_{\omega\mathrm{Estane}}$, $U_{\rho_{\mathrm{bo}}}$, U_{r_2}, U_{r_5}, and $U_{\mathrm{H_2O_a}}$.

Symbol	Name	Uncertainty Multyplier	r^c	r^2
U_{β_V}	Volumetric expansion	1±0.03	-0.078	0.006
U_{C_b}	Bulk Specific Heat	1±0.05	0.131	0.017
$U_{\mathrm{latent},\,\beta\text{-}\delta}$	Latent Enthalpy ($\beta-\delta$)	1±0.05	0.011	0.000
$U_{\mathrm{latent,\,melt}}$	Latent Enthalpy (HMX melt)	1±0.05	-0.008	0.000
U_{khi}	High temperature conductivity	1±0.05	-0.070	0.005
U_{klo}	Low temperature conductivity	1±0.05	0.006	0.000
U_{r_1}	Reaction 1	1±0.05	-0.043	0.002
U_{r_2}	Reaction 2	1±0.05	**-0.235**	**0.056**
U_{r_3}	Reaction 3	1±0.05	0.027	0.001
U_{r_4}	Reaction 4	1±0.05	-0.115	0.013
U_{r_5}	Reaction 5	1±0.05	**-0.195**	**0.038**
$U_{\rho_{\mathrm{bo}}}$	Initial Bulk density	1±0.02	**0.239**	**0.057**
$U_{T\,\beta\text{-}\delta}$	$\beta-\delta$ phase change temperature	1±0.005	0.018	0.000
$U_{T\mathrm{melt}}$	HMX melt temperature	1±0.005	-0.111	0.012
U_{Ullage}	Free gas volume	1±0.005	-0.023	0.000
$U_{\omega\mathrm{BDNPA/F}}$	BDNPA/F initial mass fraction[a]	–	**0.911**	**0.830**
$U_{\omega\mathrm{Estane}}$	Estane® initial mass fraction[b]	–	**-0.255**	**0.065**
$U_{\mathrm{H_2O_a}}$	Mass fraction of adsorbed water	1±0.10	**0.150**	**0.023**
$U_{\Sigma x\mathrm{hi}}$	BKWS covolume factor	1±0.05	-0.116	0.013
U_{ζ}	Melt rate acceleration factor	1±0.05	-0.068	0.005

[a,b]Uncertainty range was calculated as a function of the binder migration correlation, $(1.63-0.00073\times\rho_{\mathrm{bo}})\times0.025$, by varying the initial bulk density ρ_{bo} within an uncertainty random multiplyier of 1±0.05.
[c]This is Pearson's correlation coefficient.

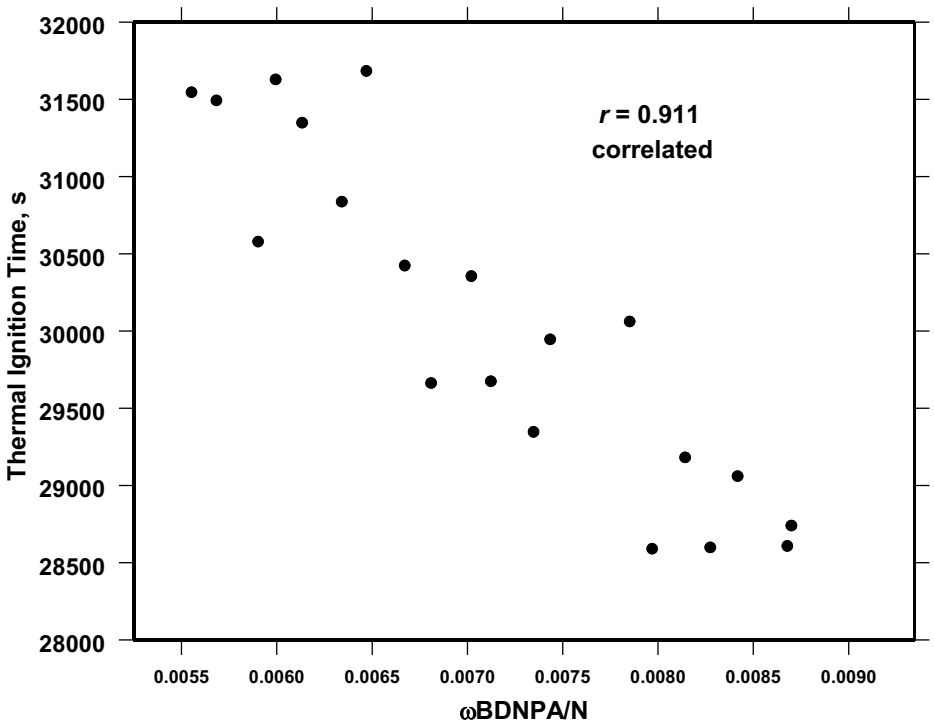

Figure 33. Thermal ignition from LHS study for LSAC shot 7 against the initial mass fraction of BDNPA/N.

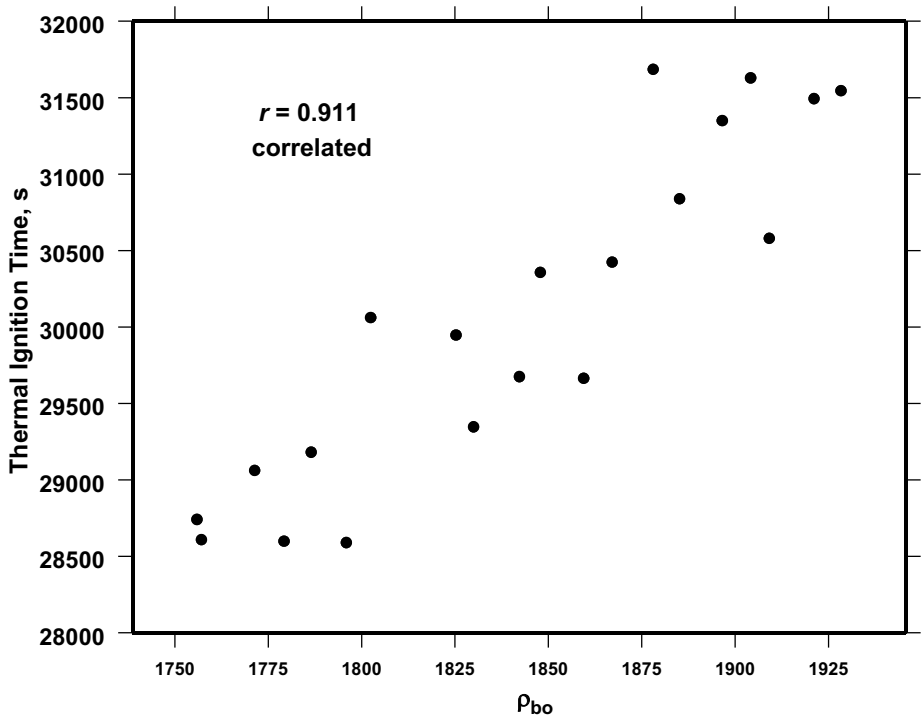

Figure 34. Thermal ignition from LHS study for LSAC shot 7 against the initial bulk density random variation considered in the binder migration correlation.

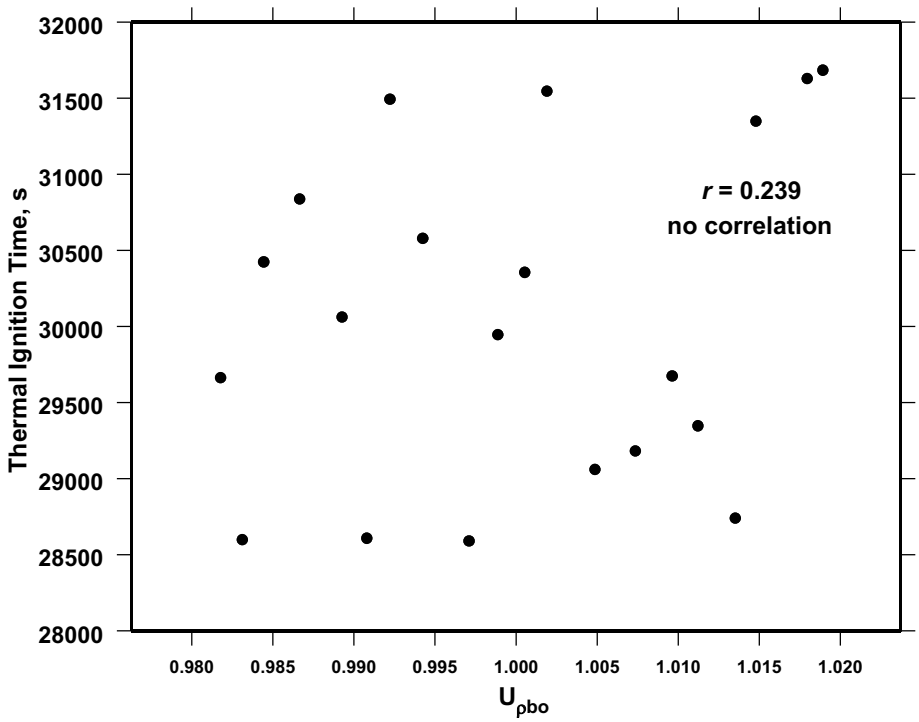

Figure 35. Thermal ignition from LHS study for LSAC shot 7 against the Initial bulk density uncertainty multiplier.

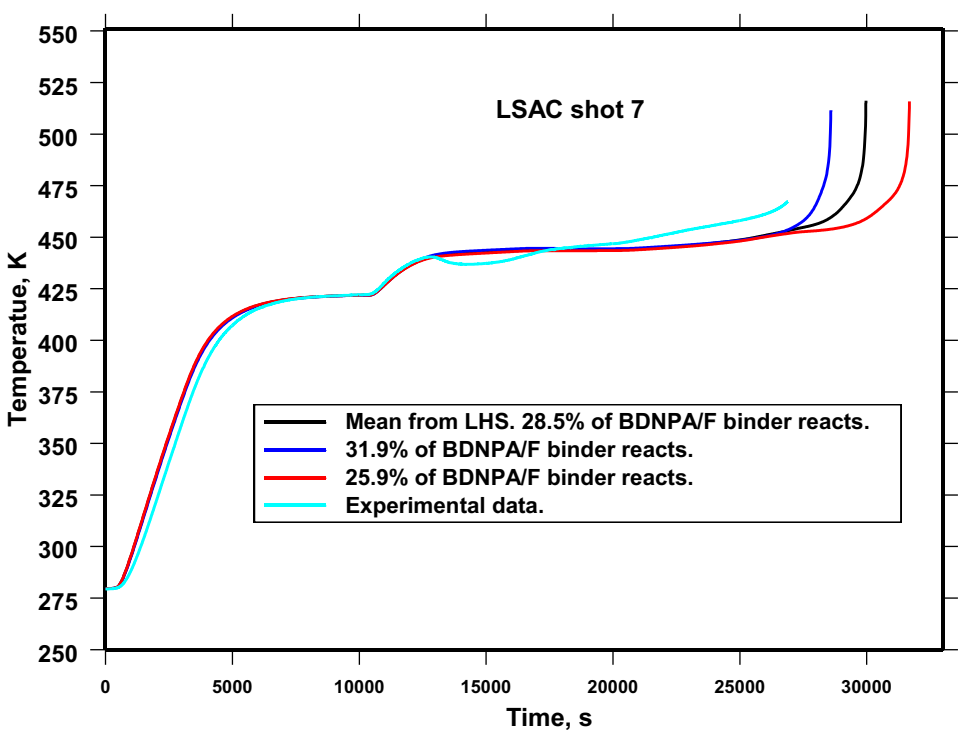

Figure 36. Upper and lower bounds, and mean from the LHS simulations of LSAC shot 7. Thermocople that measured ignition is also shown.

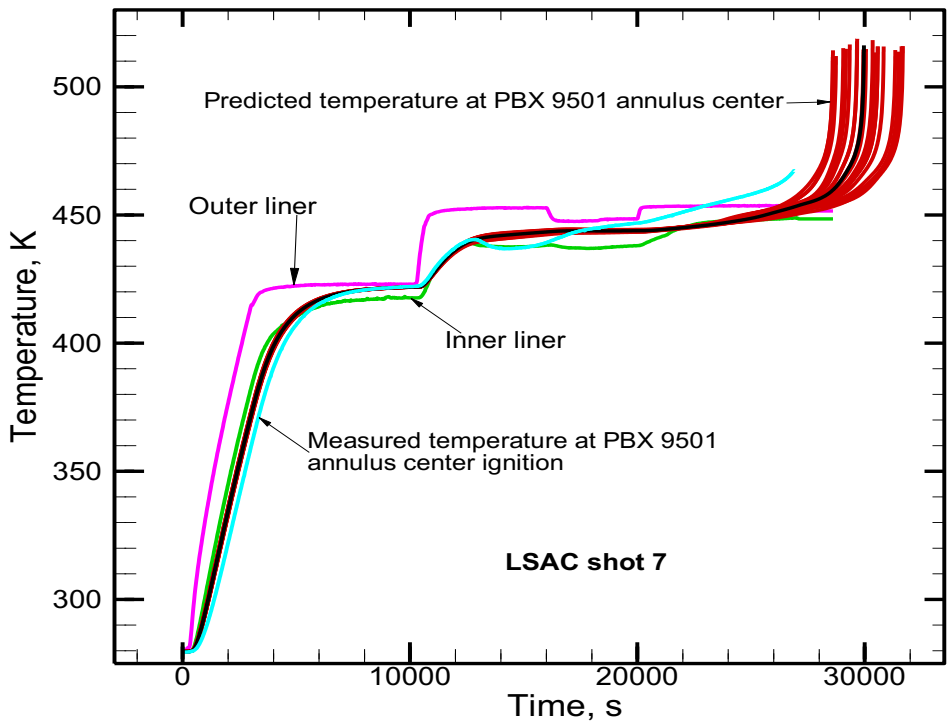

Figure 37. Simulations of 20 LHS samples using LSAC experiment shot 7.

bulk density produced by the uncertainty multiplyer contained in the binder migration correlation. Note from Fig. 34 that as the initial bulk density contained in the binder migration correlation increases, the thermal ignition time also increases which is consistent with the sign of the correlation coefficient of +0.911. Figure 35 shows the random variation of the thermal ignition time with respect to the uncertainty multiplier of the initial bulk density, $U_{\rho_{bo}}$. This plot shows no correlation for $U_{\rho_{bo}}$. Figure 36 shows a plot of the lowest ignition time, highest ignition time, and the LHS mean ignition time from the LHS simulations of LSAC shot 7. Note from Fig. 36 that the case when 31.9% of the BDNPA/F (initial ωBDNPA/F = 0.0079726) binder reacts corresponds with the lower bound of the thermal ignition time. Also, Fig. 36 shows that the case when 25.9% of the BDNPA/F binder (initial ωBDNPA/F = 0.0064730) reacts corresponds with the upper bound of the thermal ignition time. The mean of the LHS simulations for shot 7 corresponds with the case when 28.5% of the BDNPA/F binder (initial ωBDNPA/F = 0.007128) reacts in Fig. 36. Figure 37 shows the temperature results from the LHS simulations of LSAC experiment shot 7. The black curve represents the mean of the LHS simulations.

The seventh LHS sampling study was done on the LSAC shot 8. Table 13 shows the results that include the Pearson's correlation coefficient for the ignition time. The uncertainty in the initial mass fraction of the BDNPA/F had the highest correlation with a value of 0.915. This correlation is positive, which implies that the ignition time increases when the uncertainty multiplyer of the initial bulk density in the SITI binder correlation equation increases. Figure 38 plots the ignition time against the initial BDNPA/F mass fraction produced by the LHS simulations of LSAC shot 8. Figure 39 plots the thermal ignition time against the random initial bulk density produced by the uncertainty multiplyer contained in the binder migration correlation. Note from Fig. 39 that as the initial bulk density contained in the binder

Table 13. Uncertainty multipliers and correlation coefficients for LSAC experiment shot 8. The most correlated parameters are associated with the uncertainty multipyers $U_{\omega\text{BDNPA/F}}$, $U_{\rho_{\text{bo}}}$, U_{r_2}, $U_{\omega\text{Estane}}$, U_{r_5}, and $U_{\text{H}_2\text{O}_\text{a}}$.

Symbol	Name	Uncertainty Multyplier	r^c	r^2
U_{β_V}	Volumetric expansion	1±0.03	-0.083	0.007
U_{C_b}	Bulk Specific Heat	1±0.05	0.134	0.018
$U_{\text{latent, }\beta\text{-}\delta}$	Latent Enthalpy ($\beta-\delta$)	1±0.05	-0.004	0.000
$U_{\text{latent, melt}}$	Latent Enthalpy (HMX melt)	1±0.05	-0.020	0.000
U_{khi}	High temperature conductivity	1±0.05	-0.040	0.002
U_{klo}	Low temperature conductivity	1±0.05	-0.029	0.001
U_{r_1}	Reaction 1	1±0.05	-0.051	0.003
U_{r_2}	Reaction 2	1±0.05	**-0.242**	**0.059**
U_{r_3}	Reaction 3	1±0.05	0.013	0.000
U_{r_4}	Reaction 4	1±0.05	-0.112	0.012
U_{r_5}	Reaction 5	1±0.05	**-0.166**	**0.028**
$U_{\rho_{\text{bo}}}$	Initial Bulk density	1±0.02	**0.259**	**0.067**
$U_{T\,\beta\text{-}\delta}$	$\beta-\delta$ phase change temperature	1±0.005	0.011	0.000
$U_{T\text{melt}}$	HMX melt temperature	1±0.005	-0.125	0.015
U_{Ullage}	Free gas volume	1±0.005	-0.003	0.000
$U_{\omega\text{BDNPA/F}}$	BDNPA/F initial mass fraction[a]	–	**0.915**	**0.838**
$U_{\omega\text{Estane}}$	Estane® initial mass fraction[b]	–	**-0.241**	**0.058**
$U_{\text{H}_2\text{O}_\text{a}}$	Mass fraction of adsorbed water	1±0.10	**0.146**	**0.021**
$U_{\Sigma x\text{ihi}}$	BKWS covolume factor	1±0.05	-0.105	0.011
U_{ζ}	Melt rate acceleration factor	1±0.05	-0.085	0.007

[a,b]Uncertainty range was calculated as a function of the binder migration correlation, $(1.63-0.00073\times\rho_{\text{bo}})\times0.025$, by varying the initial bulk density ρ_{bo} within an uncertainty random multiplyier of 1±0.05.
[c]This is Pearson's correlation coefficient.

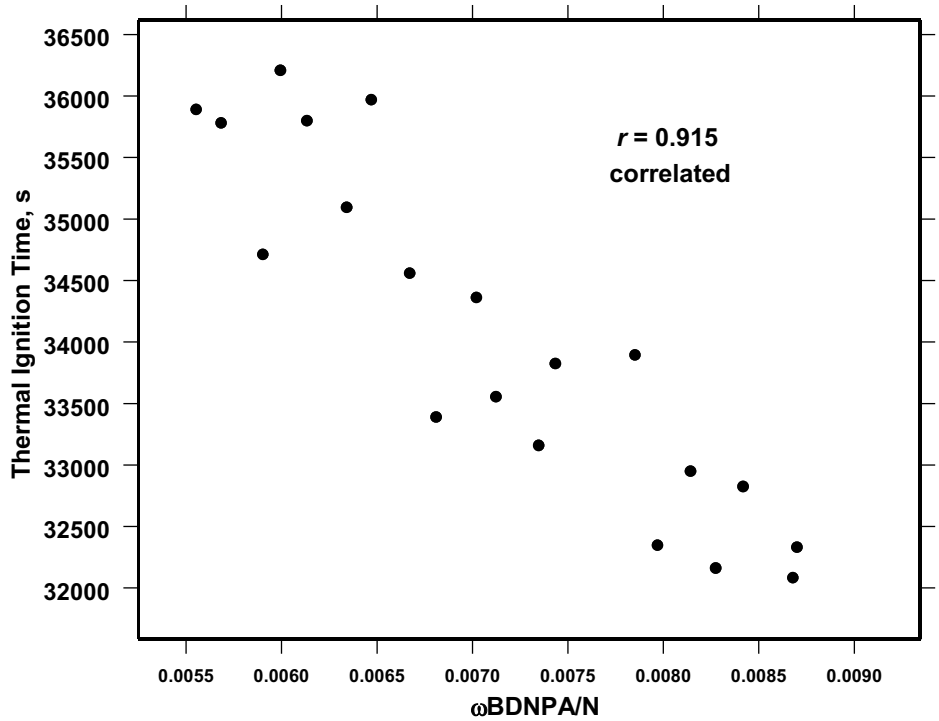

Figure 38. Thermal ignition from LHS study for LSAC shot 8 against the initial mass fraction of BDNPA/N.

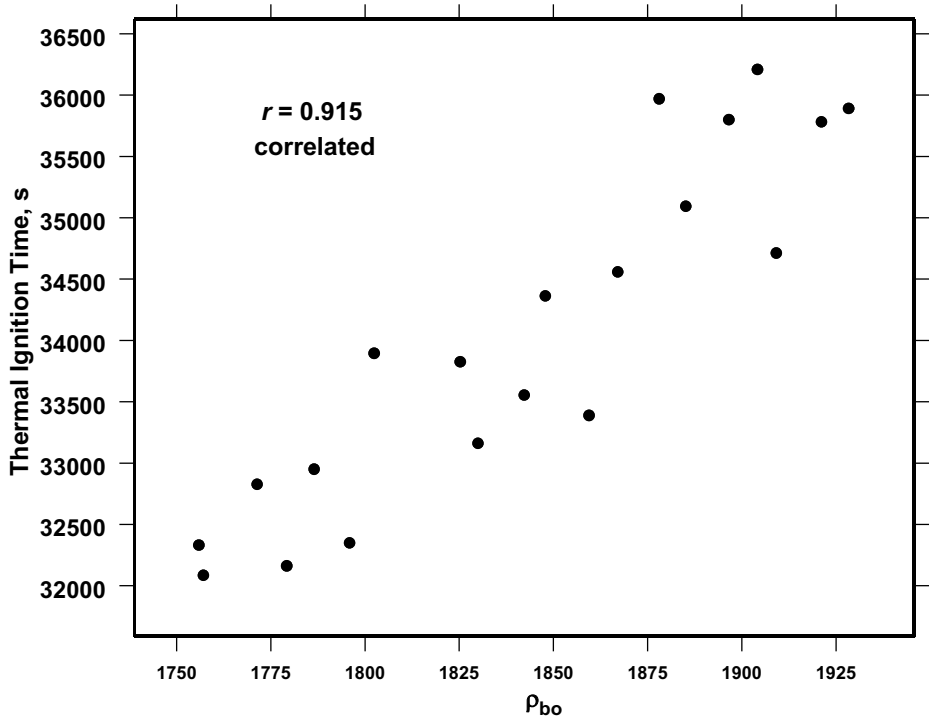

Figure 39. Thermal ignition from LHS study for LSAC shot 8 against the initial bulk density random variation considered in the binder migration

correlation.

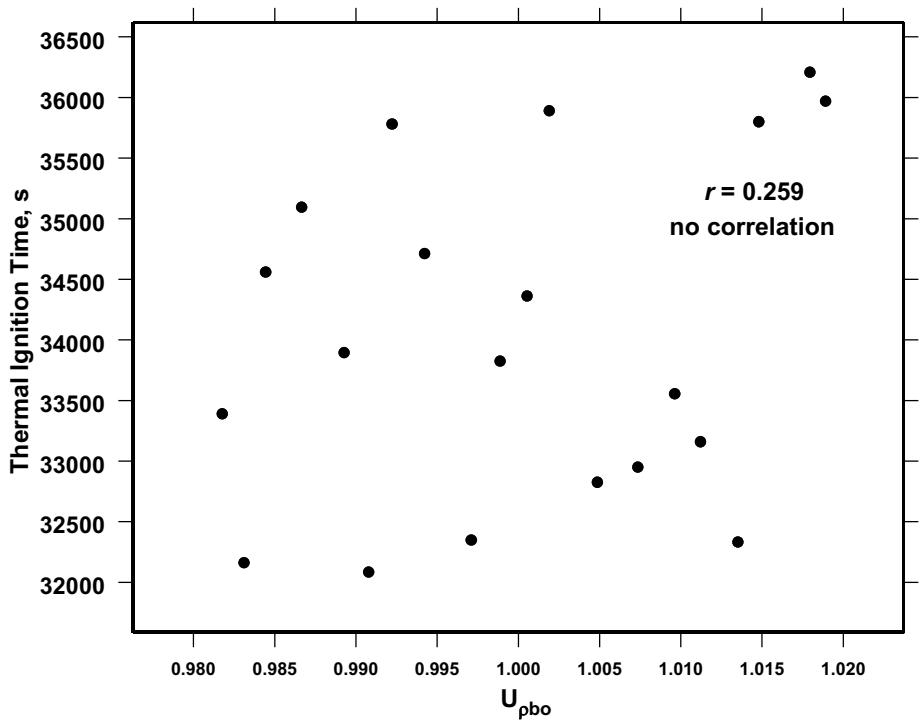

Figure 40. Thermal ignition from LHS study for LSAC shot 8 against the Initial bulk density uncertainty multiplier.

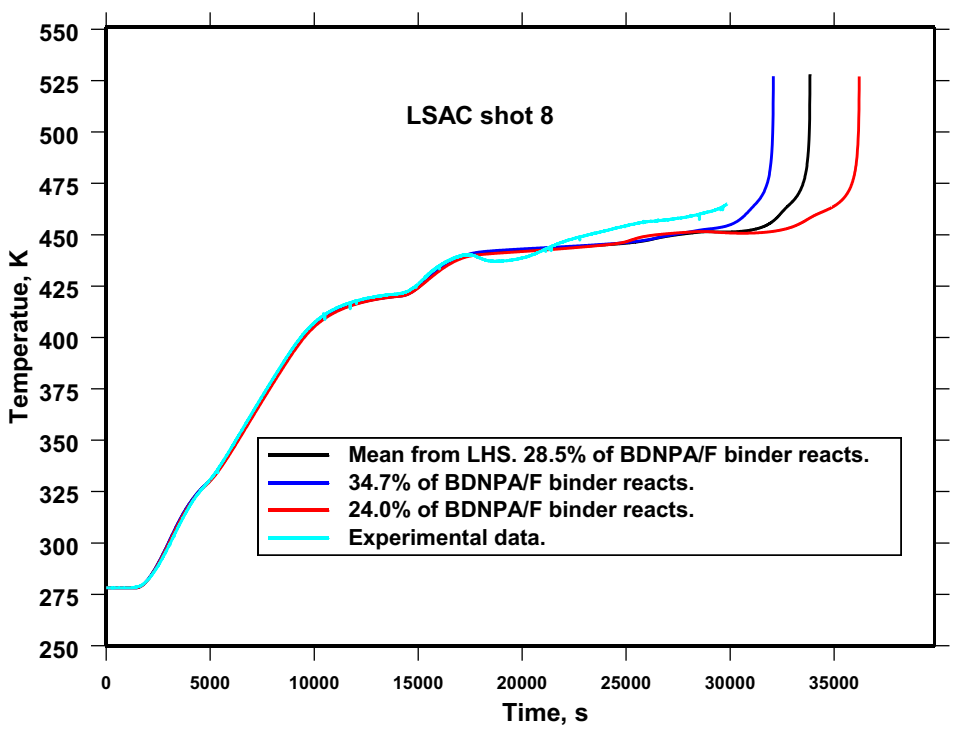

Figure 41. Upper and lower bounds, and mean from the LHS simulations of LSAC shot 8. Thermocople that measured ignition is also shown.

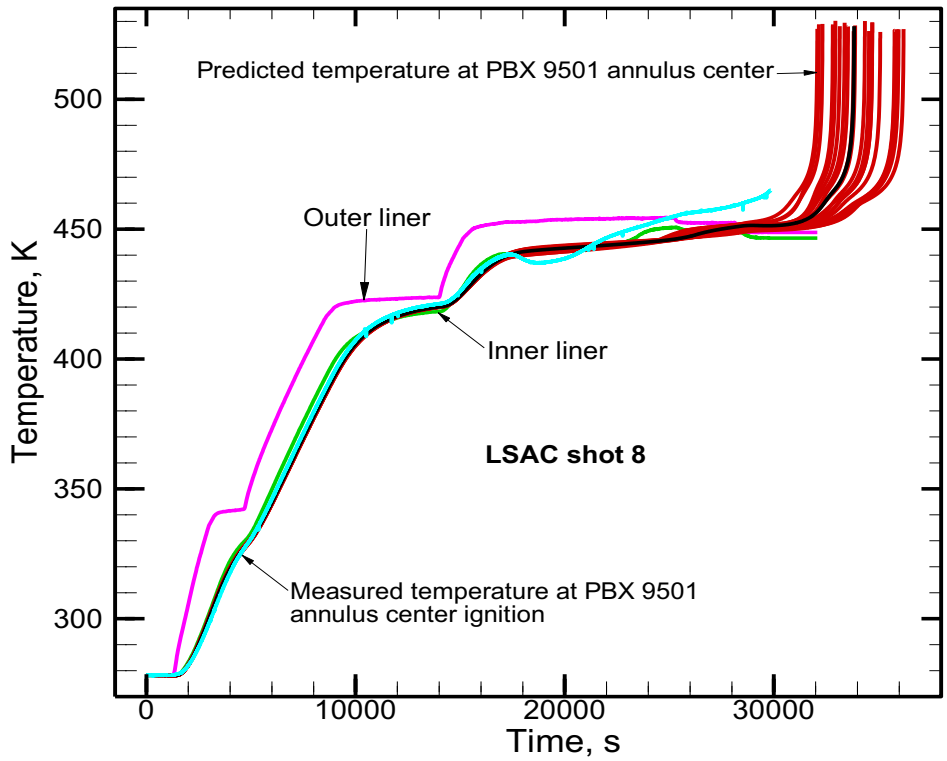

Figure 42. Simulations of 20 LHS samples using LSAC experiment shot 8.

migration correlation increases, the thermal ignition time also increases which is consistent with the sign of the correlation coefficient of +0.915. Figure 40 shows the random variation of the thermal ignition time with respect to the uncertainty multiplier of the initial bulk density, $U_{\rho_{bo}}$. This plot shows no correlation for $U_{\rho_{bo}}$. Figure 41 shows a plot of the lowest ignition time, highest ignition time, and the LHS mean ignition time from the LHS simulations of LSAC shot 8. Note from Fig. 41 that the case when 34.7% of the BDNPA/F (initial ωBDNPA/F = 0.0086807) binder reacts corresponds with the lower bound of the thermal ignition time. Also, Fig. 41 shows that the case when 24.0% of the BDNPA/F binder (initial ωBDNPA/F = 0.00599648) reacts corresponds with the upper bound of the thermal ignition time. The mean of the LHS simulations for shot 8 corresponds with the case when 28.5% of the BDNPA/F binder (initial ωBDNPA/F = 0.007128) reacts in Fig. 41. Figure 42 shows the temperature results from the LHS simulations of LSAC experiment shot 8. The black curve represents the mean of the LHS simulations.

Conclusions and Comments

The mean of the of the thermal ignition time produced by the 20 LHS simulations done for the each LSAC experiment is given in Table 14. This table shows measured and calculated averages of the time-to-ignition as well as the percent error for shots 1, 2, 3, 5, 6, 7, and 8. The range of errors is from -13.6% to +26% with an average error of 6%. The root mean squared deviation (RMSD) is 4367 s and the percent normalized RMSD is 17%. Equations (23) to (25) show how the Error in Table 5, the RMSD, and the normalized RMSD were calculated where t_c, t_m, and n are the calculated averages of the ignition times, measured ignition times, and number of experiments

respectively. Figure 43 shows the measured ignition time plotted against the LHS averages of the thermal ignition time with a linear correlation coefficient of 0.82.

$$\text{Error} = 100 \times \frac{t_c - t_m}{t_m} \tag{23}$$

$$\text{RMSD} = \sqrt{\frac{\sum_{i=1}^{n} \left(t_c - t_m \right)^2}{n}} \tag{24}$$

$$\text{Normalized RMSD} = 100 \times \frac{\text{RMSD}}{t_m^{\max} - t_m^{\min}} \tag{25}$$

Table 14. Measured ignition times and LHS averages of the predicted ignition times for the LSAC experiments.

LSAC shot #	1	2	3	5	6	7	8
Measured Ignition Time, s	25081	45535	37689	26205	20515	27090	29865
LHS Average, s	25397	39340	32901	30370	25850	30066	34041
Error, %	-1.2	-13.6	-12.7	15.9	26.0	11.0	14.0

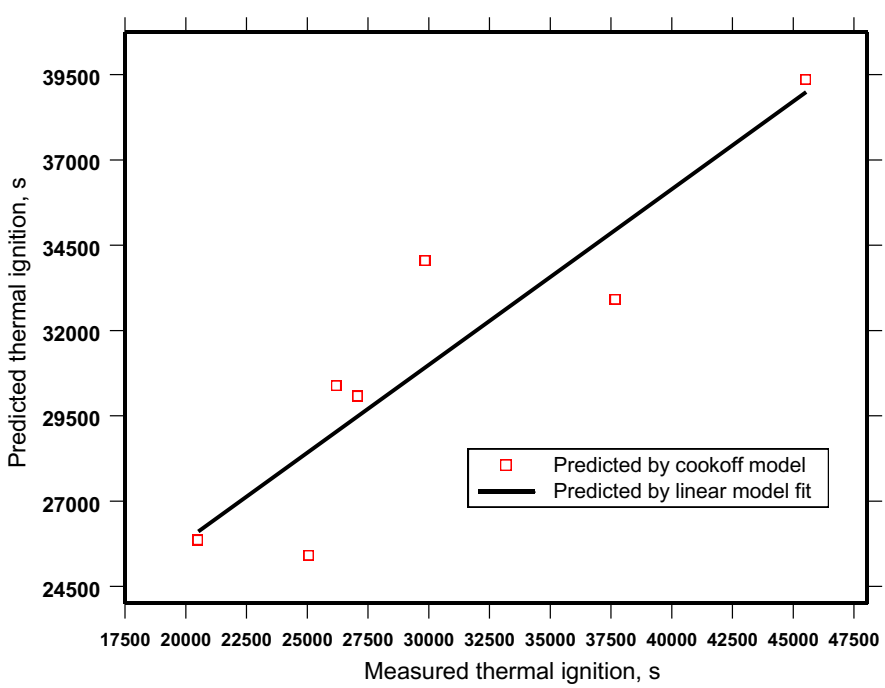

Figure 43. Measured ignition time against the LHS averages of the thermal ignition time with a linear correlation coefficient of 0.82.

The uncertainty in the initial mass fraction of the BDNPA/F was the most correlated parameter for all the LSAC experiments. There was no correlation for the rest of the parameters. Table 15 list the Pearson's correlation coefficients for initial mass fraction of the BDNPA/F.

Table 15. Most correlated parameters obtained from the LHS simulations of the LSAC experiments.

shot #	Symbol	Correlation Coefficient, *r*
1	$U_{\omega\mathrm{BDNPA/F}}$	0.914
2	$U_{\omega\mathrm{BDNPA/F}}$	0.917
3	$U_{\omega\mathrm{BDNPA/F}}$	0.919
5	$U_{\omega\mathrm{BDNPA/F}}$	0.915
6	$U_{\omega\mathrm{BDNPA/F}}$	0.912
7	$U_{\omega\mathrm{BDNPA/F}}$	0.911
8	$U_{\omega\mathrm{BDNPA/F}}$	0.915

Acknowledgements

The funding provided by Anthony Puckett (R & D Engineer, Q-15) is gratefully acknowledged.

References

[1] Hobbs, M. L., Kaneshige, M. J., Erikson, W. W., "Modeling the measured effect of a nitroplasticizer (BDNPA/F) on cookoff of a plastic bonded explosive (PBX 9501)," Combustion and Flame 173 (2016) 132–150.

[2] SIERRA Thermal/Fluid Development Team "SIERRA Multimechanics Module: Aria User Manual – Version 4.54," Sandia Report SAND2019-12296, Sandia National Laboratories, P. O. Box 5800, Albuquerque, New Mexico 87185, Livermore, California 94550, Printed October 9, 2019.

[3] Asay, B. W., Dickson, P. M., Henson, B. F., Ochwald, E., Parker, G., Perry, L., Romero, J., Smilowitz, L. B., "Large Scale Annular Cookoff Tests," LA-UR-03-3787, Los Alamos National Laboratory,P.O. Box 1663, Los Alamos, NM 87545, 2003.

[4] Behrens, R., Maharrey, S., "Chemical and physical processes that control the thermal decomposition of RDX and HMX," Int. J. Energ. Mater. Chem. Propuls. 5 (2002) 1–6.

[5] Hobbs, M. L. and Baer, M. R., "Calibrating the BKW-EOS with a Large Product Species Data Base and Measured C-J Properties," Proceedings of the 10th International Detonation Symposium, pp. 409-418, Boston, MA, July 1993.

[6] Copps, K. D. and Carnes, B. C., Sierra Verification Module: Encore User Guide – Version 4.28. SAND 2013-3344, Sandia National Laboratories, Albuquerque, NM87185, USA, June 2013.

[7] Skroch, M., Owen, S. J., Staten, M. L., Quadros, R. W., Hanks, B., Clark, B., Hensley, T., Meyers, R. J., Ernst, C., Morris, R., McBride, C., Stimpson, C., Perry, J., CUBIT, "Geometry and Mesh Generation Toolkit 15.5 User Documentation," SAND No. SAND2019-3478 W, Prepared by Sandia National Laboratories, Albuquerque, New Mexico 87185 and Livermore, California 94550.

[8] McKay, M. D., Beckman, R. J., and Conover, W. J., Technometrics 21, 239 (1979).

[9] Adams, B. M., Bauman, L. E., Bohnhoff, W. J., Dalbey, K. R., Ebedia, M. S., Eddy, J. P., Eldred, M. S., Hough, P. D., Hu, K. T., Jakeman, J. D., Swiler, L. P., Vigil, D. M., DAKOTA, A Multilevel Parallel Object-Oriented Framework for Design Optimization, Parameter Estimation, Uncertainty Quantification, and Sensitivity Analysis: Version 5.4 User's Manual, SAND2010-2183, Sandia National Laboratories, Albuquerque, NM, 2010, updated 2013.

[10] Aviles-Ramos, C. and Hobbs M. L., "Finite element implementation of two PBX 9501 cookoff models and comparisons with the LSAC cookoff experiments," LA-UR-20-27290, P.O. Box 1663, Los Alamos, NM 87545, 2020.